THE MOSFIRE DEEP EVOLUTION FIELD (MOSDEF) SURVEY: REST-FRAME OPTICAL SPECTROSCOPY FOR ~1500 H-SELECTED GALAXIES AT $1.37 \leqslant z \leqslant 3.8$

MARISKA KRIEK[1], ALICE E. SHAPLEY[2], NAVEEN A. REDDY[3,15], BRIAN SIANA[3], ALISON L. COIL[4], BAHRAM MOBASHER[3], WILLIAM R. FREEMAN[3], LAURA DE GROOT[3], SEDONA H. PRICE[1], RYAN SANDERS[2], IRENE SHIVAEI[3], GABRIEL B. BRAMMER[5], IVELINA G. MOMCHEVA[6], ROSALIND E. SKELTON[7], PIETER G. VAN DOKKUM[6], KATHERINE E. WHITAKER[8], JAMES AIRD[9], MOJEGAN AZADI[4], MARC KASSIS[10], JAMES S. BULLOCK[11], CHARLIE CONROY[12,13], ROMEEL DAVÉ[14], DUŠAN KEREŠ[4], AND MARK KRUMHOLZ[13]

[1] Astronomy Department, University of California, Berkeley, CA 94720, USA
[2] Department of Physics & Astronomy, University of California, Los Angeles, CA 90095, USA
[3] Department of Physics & Astronomy, University of California, Riverside, CA 92521, USA
[4] Center for Astrophysics and Space Sciences, University of California, San Diego, La Jolla, CA 92093, USA
[5] Space Telescope Science Institute, Baltimore, MD 21218, USA
[6] Department of Astronomy, Yale University, New Haven, CT 06511, USA
[7] South African Astronomical Observatory, PO Box 9, Observatory, Cape Town 7935, South Africa
[8] Astrophysics Science Division, Goddard Space Center, Greenbelt, MD 20771, USA
[9] Institute of Astronomy, University of Cambridge, Madingley Road, Cambridge CB3 0HA, UK
[10] W.M. Keck Observatory, Kamuela, HI 96743-8431, USA
[11] Center for Cosmology, Department of Physics and Astronomy, University of California, Irvine, CA 92697, USA
[12] Harvard-Smithsonian Center for Astrophysics, 60 Garden St., Cambridge, MA, USA
[13] Department of Astronomy & Astrophysics, University of California, Santa Cruz, CA, USA
[14] University of the Western Cape, Bellville, Cape Town 7535, South Africa

ABSTRACT

In this paper we present the MOSFIRE Deep Evolution Field (MOSDEF) survey. The MOSDEF survey aims to obtain moderate-resolution ($R = 3000$–3650) rest-frame optical spectra (~3700–7000 Å) for ~1500 galaxies at $1.37 \leqslant z \leqslant 3.80$ in three well-studied CANDELS fields: AEGIS, COSMOS, and GOODS-N. Targets are selected in three redshift intervals: $1.37 \leqslant z \leqslant 1.70$, $2.09 \leqslant z \leqslant 2.61$, and $2.95 \leqslant z \leqslant 3.80$, down to fixed H_{AB} (F160W) magnitudes of 24.0, 24.5, and 25.0, respectively, using the photometric and spectroscopic catalogs from the 3D-HST survey. We target both strong nebular emission lines (e.g., [O II] $\lambda\lambda$3727, 3730, Hβ, [O III] $\lambda\lambda$4960, 5008, Hα, [N II] $\lambda\lambda$6550, 6585, and [S II] $\lambda\lambda$6718, 6733) and stellar continuum and absorption features (e.g., Balmer lines, Ca II H and K, Mgb, 4000 Å break). Here we present an overview of our survey, the observational strategy, the data reduction and analysis, and the sample characteristics based on spectra obtained during the first 24 nights. To date, we have completed 21 masks, obtaining spectra for 591 galaxies. For ~80% of the targets we derive a robust redshift from either emission or absorption lines. In addition, we confirm 55 additional galaxies, which were serendipitously detected. The MOSDEF galaxy sample includes unobscured star-forming, dusty star-forming, and quiescent galaxies and spans a wide range in stellar mass ($\sim 10^9$–$10^{11.5}\,M_\odot$) and star formation rate ($\sim 10^0$–$10^3\,M_\odot\,\mathrm{yr}^{-1}$). The spectroscopically confirmed sample is roughly representative of an H-band limited galaxy sample at these redshifts. With its large sample size, broad diversity in galaxy properties, and wealth of available ancillary data, MOSDEF will transform our understanding of the stellar, gaseous, metal, dust, and black hole content of galaxies during the time when the universe was most active.

Key words: galaxies: distances and redshifts – galaxies: evolution – galaxies: formation – galaxies: high-redshift – surveys

1. INTRODUCTION

Understanding the formation and evolution of galaxies remains one of the greatest challenges of modern astronomy. Key outstanding questions include: What are the physical processes driving star formation in individual galaxies? How do galaxies exchange gas and heavy elements with the intergalactic medium? How are stellar mass and structure assembled in galaxies (in situ star formation versus mergers)? What is the nature of the coevolution of black holes and stellar populations?

Addressing these questions requires observations of galaxy populations across cosmic time. The Sloan Digital Sky Survey (York et al. 2000) and the 2dF Galaxy Redshift Survey (Colless et al. 2001) provide a detailed description of the local galaxy population, with imaging and spectra of more than 10^6 galaxies. These data quantify the distributions in galaxy luminosity, color, stellar, dynamical and black hole mass, structural properties, gas content, metallicity, and environment, as well as the strong correlations among these parameters. Such results provide an endpoint for our description of galaxy evolution.

In order to understand the full story from beginning to end, however, we require observations probing earlier cosmic epochs. Several spectroscopic surveys (e.g., DEEP2, VVDS, zCOSMOS, PRIMUS; Le Fèvre et al. 2005; Lilly et al. 2007; Coil et al. 2011; Newman et al. 2013) have probed the properties of galaxy populations to $z \sim 1$ with sample sizes of $\sim 10^4$–10^5 objects, describing the evolution in the luminosities,

---
[15] Alfred P. Sloan Research Fellow.

colors, stellar masses, sizes, and environments of both star-forming and quiescent galaxies over the past ~8 Gyr.

The next frontier for comprehensive galaxy surveys is the epoch at $1.5 \lesssim z \lesssim 3.5$, the peak of both star formation and black hole accretion activity in the universe (e.g., Hopkins & Beacom 2006; Reddy et al. 2008). Several qualitative imprints of the local galaxy patterns have already been observed at these earlier times, including the bimodal distribution of galaxy colors (e.g., Cassata et al. 2008; Kriek et al. 2008a; Williams et al. 2009; Whitaker et al. 2011), the strong clustering of red galaxies (e.g., Quadri et al. 2008), the mass–metallicity relation (e.g., Erb et al. 2006), and the correlation between stellar population properties and structural parameters (e.g., Williams et al. 2010; Wuyts et al. 2011a). However, there are also striking differences, such as the large diversity among massive galaxies (e.g., Kriek et al. 2009a; van Dokkum et al. 2011; Muzzin et al. 2013b) and the absence of cold, quiescent disk galaxies (e.g., Förster Schreiber et al. 2009; Law et al. 2009).

Although great strides have been made in the past several years to survey galaxies at this key epoch (see Shapley 2011 for a recent review), most studies are based on multiwavelength photometric data alone, with little or no spectroscopic information (e.g., Wuyts et al. 2011b). Rest-frame UV spectra have been measured for ~3000 galaxies at $1.5 \lesssim z \lesssim 3.5$ (Steidel et al. 2003, 2004), yet the sample of such objects is biased toward relatively blue, star-forming galaxies, and these spectra are primarily sensitive to interstellar and circumgalactic medium (ISM/CGM) features tracing outflowing gas (e.g., Shapley et al. 2003). Current surveys with the *Hubble Space Telescope* (*HST*)/WFC3 near-IR grisms are yielding rest-frame optical spectra of ~10,000 galaxies at $z > 1$ (Atek et al. 2010; Brammer et al. 2012), yet the low spectral resolution ($R < 130$) and limited wavelength range ($\lambda < 1.65\,\mu m$) prevent a robust characterization of emission and absorption line ratios and widths over the range $1.5 \lesssim z \lesssim 3.5$. Finally, moderate-resolution rest-frame optical spectroscopy has been obtained at $1.5 \lesssim z \lesssim 3.5$ for (UV-selected) star-forming galaxies (e.g., Erb et al. 2006; Mannucci et al. 2009; Förster Schreiber et al. 2009) and stellar mass-limited samples of massive galaxies ($M \geqslant 10^{11}\,M_\odot$; e.g., Kriek et al. 2008b). Yet the largest homogeneous sample obtained until recently consisted of ~100 galaxies, and the wavelength coverage and depth was in most cases insufficient to observe all strong spectral features.

Key requirements for a complete evolutionary census of the galaxy population at $1.5 \lesssim z \lesssim 3.5$ include (1) rest-frame optical spectroscopy covering all of the strongest emission and absorption features between rest-frame 3700 and 6800 Å, with sufficient resolution to characterize the gaseous and stellar contents of galaxies, (2) a large ($N > 10^3$) sample of objects, spanning the full diversity of stellar populations and dust extinction over a large dynamic range in stellar mass, and (3) multiple redshift bins to enable evolutionary studies. These requirements can now be met with the commissioning of the MOSFIRE spectrograph (McLean et al. 2010, 2012) on the Keck I telescope. KMOS (Sharples et al. 2004) on the Very Large Telescope and FMOS (Kimura et al. 2010) on Subaru are also providing near-IR spectra of large samples of distant galaxies (e.g., Wisnioski et al. 2014; Silverman et al. 2014).

MOSFIRE is a multiobject moderate-resolution spectrograph operating from 0.97 to 2.45 μm, enabling the simultaneous spectroscopic observation of ~30 individual galaxies distributed over a $6' \times 3'$ field of view. Steidel et al. (2014) demonstrate the power of MOSFIRE for studying nebular line emission using a sample of 179 star-forming galaxies at $2 < z < 3$. In addition, Belli et al. (2014) illustrate MOSFIRE's potential for continuum emission studies of distant galaxies, using a sample of six massive galaxies at $2 < z < 3$. To combine these two strengths and assemble the first true statistical and magnitude-limited spectroscopic galaxy sample at these redshifts, we are conducting the MOSFIRE Deep Evolution Field (MOSDEF) survey. We plan to obtain rest-frame optical spectra for ~1500 galaxies in the range $1.4 \lesssim z \lesssim 3.8$. Together with existing multiwavelength data, MOSDEF enables measurements of the stellar, gaseous, metal, dust, and black hole content of galaxies spanning a wider dynamic range in physical properties than has ever been accessed before with rest-frame optical spectroscopic surveys at these redshifts.

MOSDEF is being executed over 47 nights from 2012 December to the spring of 2016. In this paper we present an overview of the survey, the observational strategy, the data reduction and analysis, and the sample characteristics based on data obtained over the first 24 nights of observing. The paper is organized as follows. In Section 2 we present the MOSDEF survey design and observing strategy and an overview of the first observing runs. In Section 3 we discuss the two-dimensional (2D) data processing, the noise properties, and the extraction of the one-dimensional (1D) spectra. Section 4 describes the spectral measurements, line and continuum sensitivities, the spectroscopic success rate, the sample characteristics, and a comparison to the parent magnitude-limited sample at the same redshifts, from which targets are drawn. In Section 5 we outline the MOSDEF science objectives, and finally, in Section 6 we present a summary.

Throughout this work we assume a ΛCDM cosmology with $\Omega_m = 0.3$, $\Omega_\Lambda = 0.7$, and $H_0 = 70$ km s^{-1} Mpc^{-1}. All magnitudes are given in the AB-magnitude system (Oke & Gunn 1983). The wavelengths of all emission and absorption lines are given in vacuum.

2. OBSERVATIONS

2.1. Survey Design

In order to quantify galaxy evolution within the MOSDEF survey, we target three redshift ranges: $1.37 \leqslant z \leqslant 1.70$, $2.09 \leqslant z \leqslant 2.61$, $2.95 \leqslant z \leqslant 3.80$. The targeted redshift regimes are selected such that bright rest-frame optical emission lines fall within atmospheric windows, as illustrated in Figure 1. A key aspect of our survey strategy is that we cover multiple rest-frame optical emission lines for each galaxy. Thus our strategy requires two or three filters per slit mask. For the $1.37 \leqslant z \leqslant 1.70$ interval, we target Hβ and [O III] in the J band and Hα, [N II], and [S II] in the H band. Within this window, we also target [O II] in the Y band for $1.61 \leqslant z \leqslant 1.70$. These same features appear in J, H, and K for the $2.09 \leqslant z \leqslant 2.61$ interval. For the $2.95 \leqslant z \leqslant 3.80$ interval, [O II] falls in the H band, and Hβ and [O III] in the K band. We also target several continuum features and absorption lines in each of our three redshift regimes, including the 4000 Å break, Ca II H and K, Mgb at 5178 Å, and Balmer absorption lines.

Emphasis is given to the middle-redshift regime ($2.09 \leqslant z \leqslant 2.61$), in which we plan to obtain a total sample of ~750 galaxies. In the low- and high-redshift ranges, together, we aim to target ~750 galaxies as well, with the
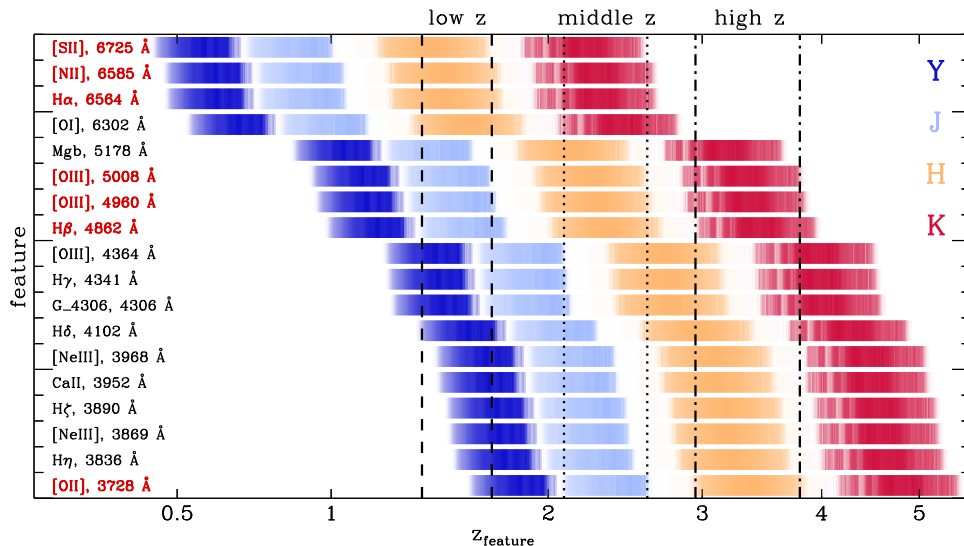
Figure 1. MOSFIRE visibility of various rest-frame optical emission and absorption features as a function of redshift. Each row represents a different spectral feature, as indicated on the left. The primary emission-line features are indicated in bold red. Each color represents a different filter, as indicated in the top right. The response curves are used for each filter and feature, and thus the brightness reflects the relative throughput at the corresponding redshift. The MOSDEF low ($1.37 \leqslant z \leqslant 1.70$), middle ($2.09 \leqslant z \leqslant 2.61$), and high ($2.95 \leqslant z \leqslant 3.80$) redshift intervals are indicated by the dashed, dotted, and dash-dotted vertical lines, respectively. This figure illustrates that the MOSDEF survey covers key emission features in each target redshift interval.
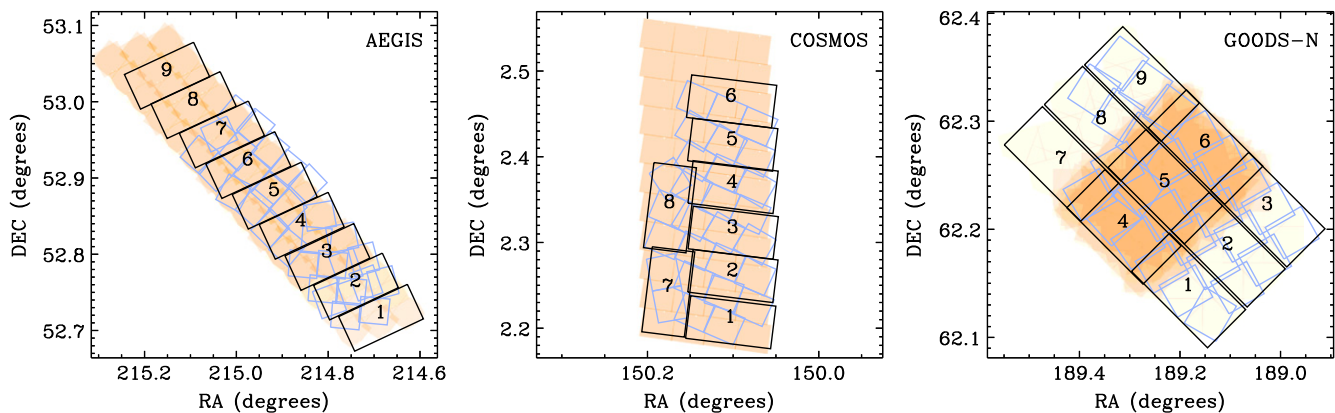

Figure 2. Footprints of MOSDEF observations in the primary target fields. From left to right we show the AEGIS, COSMOS, and GOODS-N fields. The MOSFIRE pointings and corresponding numbers are indicated in black. Each MOSFIRE pointing is $3' \times 6'$. The shaded orange regions represent the CANDELS *HST* WFC3/F160W exposure maps, and the open light-blue boxes represent the 3D-*HST* WFC3/G141 grism pointings.

sample being roughly equally split between the two intervals. As each redshift interval requires different filter combinations, we use different masks for each interval. Nonetheless, we include targets from the other redshift intervals as fillers as space allows on each mask. The total planned area is ~600 square arcminutes for the middle-redshift regime, and ~300 square arcminutes for the lower and higher redshift regimes.

The MOSDEF survey is primarily being executed in three well-studied legacy fields with deep, extensive multiwavelength data sets: AEGIS (Davis et al. 2007), COSMOS (Scoville et al. 2007), and GOODS-N (Giavalisco et al. 2004). During the first observing season we also observed one mask in UKIDSS-UDS (Lawrence et al. 2007) and one mask in GOODS-S (Giavalisco et al. 2004) because our primary target fields were not visible during the first half of the night. Within all fields we target the regions that are covered by the CANDELS (Grogin et al. 2011; Koekemoer et al. 2011) and 3D-HST (Brammer et al. 2012) surveys, as illustrated in Figure 2 for the three primary fields.

Targets are selected using photometric catalogs and grism spectra as provided by the 3D-HST collaboration. These catalogs contain all public photometric data and spectroscopic redshifts available for the MOSDEF survey fields. A description of the photometric catalogs is given in Skelton et al. (2014), and the grism spectra are described in Brammer et al. (2012). The grism redshifts are derived by fitting the grism spectra and multiwavelength photometry simultaneously (Brammer et al. 2012, 2013; I. Momcheva et al. 2015, in preparation). Additional spectroscopic redshifts are included as well (Reddy et al. 2006; Barger et al. 2008; Coil et al. 2009, 2011; Cooper et al. 2012; Newman et al. 2013; van de Sande et al. 2013). When no spectroscopic redshift is available, from either the grism spectra or other spectroscopic campaigns, we use a photometric redshift as derived using EAzY (Brammer et al. 2008).

Within each redshift interval we select by H-band (F160W) magnitude. The magnitude limits are $H = 24.0$, $H = 24.5$, and $H = 25.0$, for the lower, middle, and higher redshift intervals, respectively. For these limits, we obtain a roughly consistent

stellar mass limit of $\sim 10^9 \, M_\odot$ in each redshift interval. The 3D-*HST* catalogs used for the selection are F125W+F140W+F160W-selected, and Skelton et al. (2014) show that the catalogs are 90% complete at a magnitude of $H = 25$ for the shallow CANDELS data. GOODS-N is complete to a fainter magnitude. The H band covers the rest-frame optical wavelength regime out to $z \sim 3.8$, and thus we target a wide range in galaxy spectral energy distributions (SEDs). However, as discussed in Section 4.6, this selection will slightly bias our sample to unobscured star-forming galaxies with lower mass-to-light ratios (M/L_H) in the H band. Nonetheless, within the star-forming population, the rest-optical is less biased to recent bursts of star formation, as changes in M/L_H are small compared to changes in the equivalent widths of the nebular emission lines or the UV and infrared continua (e.g., Domínguez et al. 2014).

To increase the success rate of our survey, we prioritize by magnitude and redshift when selecting targets for spectroscopy. The initial priority scales with H-band magnitude, such that brighter galaxies have a higher priority. This criterion ensures that we obtain spectra of the rare, massive galaxies and that our sample is not dominated by the far more numerous galaxies near the flux limit. Within a given magnitude bin we further prioritize by redshift. The highest priority is given to galaxies with robust spectroscopic redshifts, from either grism emission lines or other spectroscopic campaigns. Next, we prioritize galaxies that have grism redshifts (without emission lines) or photometric redshifts in the middle of the redshift intervals: $1.42 \leqslant z \leqslant 1.65$, $2.20 \leqslant z \leqslant 2.50$, and $3.05 \leqslant z \leqslant 3.70$. The lowest priority is given to galaxies with photometric redshifts at the edges of each interval. Within the lowest redshift interval, we further prioritize galaxies at $1.61 \leqslant z \leqslant 1.70$, for which [O II] is expected in the Y band. Within a specific magnitude and redshift bin, we upweight galaxies that host an active galactic nucleus (AGN), identified either by IRAC colors (Donley et al. 2012) or by a strong X-ray counterpart. Details on the AGN selection are discussed in Coil et al. (2015). Finally, for each target, we inspect the F160W image, broadband SED, best-fit stellar population model, and grism spectrum when available. In cases where the target looks unreliable (e.g., very noisy photometry, mismatch between the photometry and the best-fit stellar population model, mis-identified grism lines), it is replaced by another target during mask design (see next section). On average we replaced one to two targets per mask. However, the exact number depends on the photometric depth, which varies with field and targeted redshift interval.

2.2. Observing Strategy

Our survey is being executed with MOSFIRE (McLean et al. 2012) on the Keck I telescope. MOSFIRE is a multiobject near-IR spectrograph with an effective field of view of $3'$ by $6'$. MOSFIRE has a cryogenic configurable slit unit (CSU), consisting of 46 pairs of bars of $7\rlap{.}''1$ length each. The bars can be configured in the horizontal direction anywhere within the field and can be combined in the vertical direction with adjacent bars to make longer slits. We design our masks using the MAGMA[16] slit mask design software and adopt a slit width of $0\rlap{.}''7$. This slit width results in a spectral resolution of $R = 3400, 3000, 3650,$ and 3600 for Y, J, H, and K,

respectively. The wavelength coverage with a minimum of 5% transmission is 0.962–1.135 μm, 1.142–1.365 μm, 1.450–1.826 μm, and 1.897–2.427 μm, for Y, J, H, and K, respectively. The actual wavelength coverage of the spectra depends on the horizontal position of the slit in the CSU, and thus it differs slightly among the different targets.

We use an ABA$'$B$'$ $(+1\rlap{.}''5, -1\rlap{.}''2, +1\rlap{.}''2, -1\rlap{.}''5)$ dither pattern in order to increase the signal-to-noise ratio (S/N) of the final spectra and to account for sky variations and detector defects (see Kriek et al. 2008b). However, during the first observing run we also experimented with an ABBA dither pattern (see note to Table 1). The maximum offset for both of our dither sequences is $3''$. We set the dither space parameter in the MAGMA software to $2\rlap{.}''5$, with the result that the center of each target is at least $0\rlap{.}''8$ from the edge of each slit. Whereas in principle 46 objects can be observed at the same time, this small dither space and the distribution of targets on the sky allow us to observe on average 28 galaxies per mask, resulting in the assignment of multiple pairs of bars for some slits.

We adopt the individual exposure times recommended by the MOSFIRE instrument team: 180, 120, 120, and 180 s, respectively, for Y, J, H, and K. Using Fowler sampling with 16 readouts, these integration times result in background-limited observations. The corresponding gain and readout noise are 2.15 e-/cts and 5.8 e-, respectively. The total nominal integration times are 1 hr per filter for the $z \sim 1.5$ masks, and 2 hr per filter for the $z \sim 2.3$ and $z \sim 3.3$ masks.

We use a minimum of five alignment stars to acquire the slit masks with an H-band magnitude between 18 and 21. However, stars with $H > 20.5$ were too faint to be used for the alignment when conditions were nonoptimal in terms of seeing and transparency. All but one of the star boxes are replaced by science slits after alignment. A slit is configured on the remaining star in order to monitor the image quality, throughput, and pointing accuracy. These slit stars are also essential for the final flux calibration of the spectra (see Section 3). For our pilot observing run in 2012 December we required an H-band magnitude of $H < 20.5$ for the slit stars. However, we determined this limit to be too faint and adjusted it to $H \lesssim 20$ from 2013A onward.

We observe B8-A1 V stars at least two times throughout the night at air masses similar to those of the science observations, in order to derive a response spectrum for each band and correct for telluric absorption features. During 2012B and 2013A, telluric stars were observed with a three-bar slit in the center of the CSU. However, for the H and K bands, the telluric spectrum acquired in this manner does not cover the entire wavelength range targeted for all objects. To address this problem, we used a new mask configuration in 2014A, which has two three-bar slits that are offset in the X direction, with an alignment box in the center.[17] Together, these slits fully cover the targeted wavelength range. Dome flats are obtained for each mask and each filter as well. In the K band we also obtain neon and argon arc observations, which are needed for the wavelength calibration at the long-wavelength edge of the band.

---

[16] http://www2.keck.hawaii.edu/inst/mosfire/magma.html

[17] For readers who are interested in using this configuration when obtaining telluric star spectra, the associated mask name is "long2pos."

Table 1
Mask Overview and Observations

| Mask[a] | Mask Parameters | | | Integration Times[b] (minutes) | | | | FWHM Seeing[c] (″) | | | | 3σ depth[d] (AB mag) | | | | N_g[e] |
	R.A. (hh:mm:ss)	Decl. (dd:mm:ss)	P.A. (deg)	Y	J	H	K	Y	J	H	K	Y	J	H	K	
$z \sim 1.5$																
ae1_01	14:18:45.13	52:43: 4.62	290.05	59.6	59.6	59.6	⋯	0.62	0.52	0.54	⋯	21.8	21.8	21.5	⋯	28
ae1_05	14:19:39.72	52:52:37.07	290.38	71.6	127.2	95.4	⋯	0.97	0.80	0.77	⋯	21.5	21.9	21.2	⋯	28
co1_03	10: 0:24.43	2:18:38.86	78.05	⋯	153.1	157.1	⋯	⋯	0.79	0.90	⋯	⋯	21.7	21.4	⋯	29
co1_05	10: 0:24.84	2:24:57.96	79.04	⋯	87.5	55.7	⋯	⋯	0.87	0.83	⋯	⋯	21.4	21.3	⋯	26
gn1_04	12:37:10.32	62:11:58.99	49.29	59.6	59.6	59.6	⋯	0.61	0.55	0.54	⋯	21.8	21.7	21.6	⋯	27
ud1_01	2:17:36.71	−5:12:13.90	37.10	62.6	67.6	59.6	⋯	0.99	0.52	0.65	⋯	20.7	21.4	21.1	⋯	33
$z \sim 2.3$																
ae2_03	14:19:13.54	52:47:51.46	297.64	⋯	119.3	119.3	152.1	⋯	0.80	0.55	0.67	⋯	21.4	21.7	21.0	27
ae2_04	14:19:25.40	52:50:14.18	295.33	⋯	119.3	119.3	119.3	⋯	0.71	0.63	0.72	⋯	21.6	22.0	21.1	29
ae2_05	14:19:36.52	52:52:29.47	291.04	⋯	123.3	119.3	119.3	⋯	0.77	0.76	0.76	⋯	21.9	22.1	21.1	29
co2_01	10: 0:24.77	2:12:24.66	78.38	⋯	119.3	119.3	244.6	⋯	0.61	0.49	0.63	⋯	21.9	22.2	21.3	31
co2_03	10: 0:24.13	2:18:28.36	90.30	⋯	113.3	119.3	104.4	⋯	0.64	0.58	0.63	⋯	21.9	22.4	21.2	25
co2_04	10: 0:24.03	2:21:53.56	79.37	⋯	115.3	119.3	119.3	⋯	0.54	0.56	0.49	⋯	22.0	22.1	21.6	27
gn2_04	12:37:15.91	62:12:10.99	47.31	⋯	119.3	119.3	119.3	⋯	0.63	0.66	0.50	⋯	22.1	21.8	21.4	27
gn2_05	12:36:59.42	62:14:31.79	43.02	⋯	119.3	119.3	122.3	⋯	0.73	0.67	0.48	⋯	21.8	21.8	21.4	28
gn2_06	12:36:39.03	62:16:41.42	41.04	⋯	123.3	119.3	119.3	⋯	0.69	0.65	0.75	⋯	22.0	21.8	21.1	28
gs2_01	3:32:30.94	−27:43: 4.41	74.40	⋯	⋯	71.6	116.3	⋯	⋯	0.62	0.81	⋯	⋯	21.4	20.8	26
$z \sim 3.3$																
ae3_04	14:19:29.54	52:50:22.38	293.02	⋯	⋯	119.3	119.3	⋯	⋯	0.73	0.59	⋯	⋯	22.1	21.4	31
co3_01	10: 0:24.87	2:12:28.66	77.90	⋯	⋯	111.3	134.2	⋯	⋯	0.68	0.67	⋯	⋯	21.7	20.8	29
co3_04	10: 0:24.56	2:21:43.56	87.95	⋯	⋯	119.3	119.3	⋯	⋯	0.73	0.71	⋯	⋯	22.2	21.4	29
co3_05	10: 0:24.03	2:24:56.96	78.05	⋯	⋯	115.3	119.3	⋯	⋯	0.82	0.56	⋯	⋯	21.7	21.6	30
gn3_06	12:36:40.56	62:16:43.02	42.36	⋯	⋯	119.3	119.3	⋯	⋯	0.58	0.66	⋯	⋯	21.9	20.9	24
Total				253	1626	2216	1947									591

Note. Masks ud1_01, gs2_01, and co3_01 were observed using an ABBA dither pattern in all bands. All other masks were observed using the ABA′B′ dither pattern.
[a] The mask names include the targeted field, with ae: AEGIS; co: COSMOS, gn: GOODS-N, gs: GOODS-S, and ud: UDS, the targeted redshift with 1: $1.38 \leqslant z \leqslant 1.70$, 2: $2.09 \leqslant z \leqslant 2.61$, and 3: $2.95 \leqslant z \leqslant 3.80$, and the pointing as presented in Figure 2.
[b] The integration time only includes frames that have been used in the reduction.
[c] The FWHM of the seeing, measured from the slit star profile in the reduced spectra.
[d] Measured from the noise frame of the reduced data, using optimal extraction and the slit star profile. Thus the quoted depths are for a faint point source only.
[e] Number of targeted galaxies per mask. This number does not include serendipitous detections or slit stars.

2.3. First Data

The MOSDEF survey is planned to be executed over four spring semesters, from 2013 until 2016. Including the pilot run on 2012 December 22–24, the MOSDEF survey has been allocated 24 nights in 2012–2014, with 23 additional nights planned in 2015 and 2016. Of the 24 nights in 2012–2014, we obtained usable data during 14.5 nights. Two nights were lost because of technical problems; another 7.5 nights were lost because of poor weather conditions, during which no useful observations were obtained.

Table 1 provides an overview of the masks observed, of which six target the lower redshift regime, 10 the middle redshift regime, and five the higher redshift regime. The mask names include the target field (ae: AEGIS, co: COSMOS, and gn: GOODS-N), the redshift interval (1:$1.37 \leqslant z \leqslant 1.70$, 2: $2.09 \leqslant z \leqslant 2.61$, and 3:$2.95 \leqslant z \leqslant 3.80$), and the pointing number (see Figure 2). For our pilot observing run in 2012 December, we also observed two masks in additional CANDELS/3D-HST fields: one in GOODS-S (gs) and one in UDS (ud). The number of targeted galaxies per mask ranges

from 24 to 33, with an average of 28 galaxies. The 21 masks observed to date have resulted in 591 2D galaxy spectra. This number does not include the 122 additional objects that serendipitously fell on slits and for which 1D spectra were extracted (see Section 3.6).

Table 1 also gives the mask parameters for each mask, which include the right ascension (R.A.), declination (decl.), and the position angle (P.A.) of the CSU. The slits are tilted by 4° relative to the CSU. Because of the fixed angle of the slits, we observe galaxies at random orientations compared to their major axes. Because of the random slit orientations and the small sizes of most galaxies, only ∼25% of the galaxies exhibit resolved velocity information in their emission lines (S. Price et al. 2015, in preparation). The actual mask parameters differ slightly from the pointings presented in Figure 2 because we allow the P.A. to vary by ±5° and the mask center to vary by ±10″ in the x and y directions when finding the optimal mask configuration. However, because the optimal parameters for one pointing differ per redshift interval, we only show the nominal parameters for each pointing in Figure 2.

In addition to the mask parameters, Table 1 also gives the integration time, seeing, and depth of all masks and filters (see Section 3 for the measurement procedure). The seeing values are derived from the profiles of the slit stars in the final reduced and combined frames. However, because in our reduction procedure the poor-weather frames have a lower weight, the actual seeing variations are larger than the spread in Table 1 and are in the range 0″.4–1″.6. Thus, the values listed for the seeing are the effective seeing measurements for the corresponding mask. The depth is also measured in each final reduced frame, as explained in Section 4.2.

While our nominal integration times are 1 hr per filter for the $z \sim 1.5$ masks and 2 hr per filter for the $z \sim 2.3$ and $z \sim 3.3$ redshift masks, the actual integration times deviate in many cases. This difference is due to scheduling constraints (e.g., end of night), the removal of problematic frames, or poor weather conditions. The total integration time is just over 100 hr.

During mediocre but still observable weather conditions, priority was given to dedicated low-redshift "bad weather" masks: ae1_05, co1_03, and co1_05. By increasing the integration times, we reached depths almost comparable to those of the typical masks. However, because the weather is unpredictable, several "good weather" masks were observed during nonoptimal weather conditions as well. Consequently, the depth for similar exposure times is variable (see Table 1).

To reach our goal of ∼1500 galaxies, we plan to observe seven, 17, and eight more $z \sim 1.5$, $z \sim 2.3$, and $z \sim 3.3$ redshift masks, respectively. These additional observations will bring the total number of masks to 13, 27, and 13 for the respective redshift intervals. For the middle-redshift regime, we aim to complete all 26 pointings shown in Figure 2, in addition to the pointing in GOODS-S, which is not shown in this figure. For the other redshift intervals, we will observe roughly half of the pointings indicated in Figure 2.

3. DATA REDUCTION

3.1. 2D Data Reduction

The MOSFIRE data were reduced using a custom software package written in IDL, which produces 2D reduced spectra from raw data in a fully automatic fashion. In summary, this package removes the sky, identifies and masks cosmic rays and bad pixels, rectifies the frames, combines all individual exposures, corrects for the telluric response, and performs an initial flux calibration. The program relies on a short parameter file that lists the raw data directory, the target name (from the star list), the mask name, the MAGMA directory, and the filter. For flux calibration, one can also specify directories pointing to the response curves and the photometric catalog from which the targets were selected (see Section 3.2).

We start by identifying all relevant frames, using the header information and the parameter file. In addition to all science and calibration frames, we also identify the sky frames to be used for each science frame. This identification is based on the dither offset and the time difference between two consecutive frames. For example, the first frame of a sequence only has one sky frame, while a central exposure has two sky frames for an ABA′B′ dither pattern. For an ABBA dither pattern there is only one sky frame for each science frame. The headers also indicate which pair of bars belong to which slit. Finally, using the MAGMA files, we assign a 3D-HST ID number to each slit, identify which of the slits target stars, and obtain an initial

estimate of the wavelength calibration based on the horizontal position of the slit in the CSU.

Using the information collected in the first step, we perform an initial sky correction on each raw science frame. If only one sky frame is identified, we simply subtract the sky from the science frame. In cases for which two sky frames are identified, we subtract the average of the two adjacent sky frames. We also make a master sky and master flat frame for each filter and mask. The master sky frame is constructed by taking the median of all raw science frames[18] and will be used for the wavelength calibration. The master flat frame is constructed by averaging the individual dome flat exposures. For each science exposure we construct a master mask, in order to mask bad pixels and cosmic rays while combining the individual frames. The bad pixel map is adopted from the official MOSFIRE reduction pipeline, constructed by N. Konidaris. A cosmic-ray map is constructed for each science frame separately, by running the L.A.Cosmic routine (van Dokkum 2001) on the sky-subtracted science frame. We then combine the cosmic-ray masks with the bad pixel map to make a master mask for each science frame.

Using the master flat, we correct all sky-subtracted science frames for sensitivity differences. We do not correct the flat for the response in wavelength direction because it differs slightly among the different slits. By retaining the flat response, we can later correct for these differences (see Section 3.2).

Next, we derive all information needed to rectify the raw spectra. This procedure consists of several steps. However, for an optimal reduction, it is crucial to resample the data as few times as possible. Thus, we combine the results of all steps into one transformation, which rectifies each raw frame to the same reference coordinate system. The reference coordinate systems have the same dispersion and pixel scale (0″.1799 per pixel) as the raw frames, with the wavelength and spatial direction oriented along the x and y directions, respectively.

In the first step of the rectification procedure, we use the master flat frame to identify the edges of each spectrum. We encounter two challenges regarding the edge tracing. First, when two neighboring slits are very close in horizontal position, the dividing line between the two spectra cannot be accurately determined. In this case, the slit edges are calculated using the upper edge of the top slit and the lower edge of the bottom slit. Second, the bottom slit on each mask has been cut off, and thus we cannot accurately measure the bottom edge. Thus, the rectification for this spectrum may not be optimal.

In the second step of the rectification procedure, we straighten all spectra in the master sky frame using the slit edges and measure the positions of bright sky lines. To assign a wavelength to each position and thus solve for $\lambda(x, y)$, we fit a 2D polynomial to the x and y positions of the sky lines using the IDL function SFIT with a maximum degree of three for both dimensions combined.[19] This step is automated, as the horizontal position of a slit provides us with a rough estimate of the wavelength solution. For the K-band exposures we use argon and neon arc frames as well because there are no bright sky lines beyond 2.3 μm. The master sky and arc frames are

---

[18] There is typically no flexure, and thus sky lines stay at the same position in all raw frames for a specific mask and filter.

[19] We fit the function $\lambda(x, y) = a + by + cy^2 + dy^3 + ex + fxy + gxy^2 + hx^2 + ix^2y + jx^3$, with x the horizontal and y the vertical position of the sky lines in the spectrum rectified using the slit edges. No term has a combined x and y power higher than three.
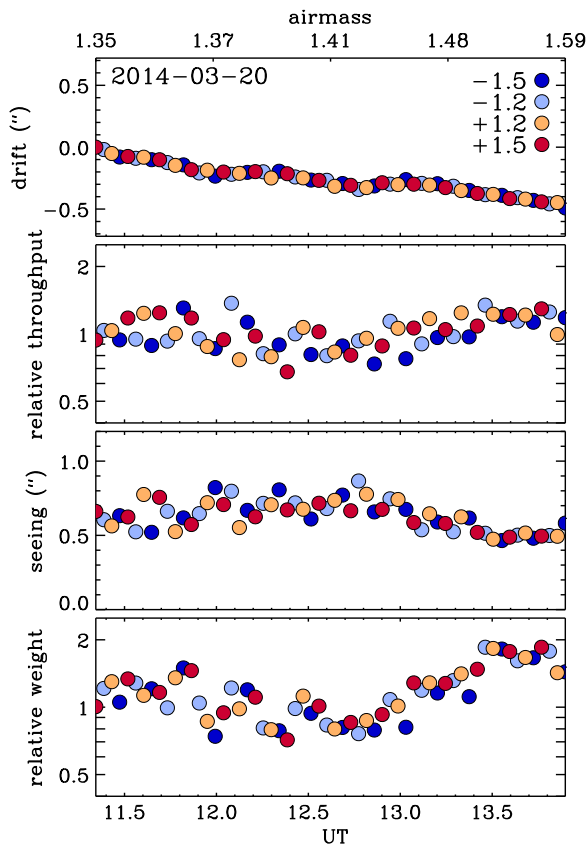
Figure 3. Slit star statistics for the J-band observations of mask gn2_04 as a function of universal time (UT) and airmass. Each dot represents an individual frame, and each color indicates a different dither position. For each mask and each frame we model the slit star profile with a Gaussian in a preliminary rectified frame. From this Gaussian we determine the relative position (drift), throughput, seeing, and weight. In the top panel we show the position compared to the first frame corrected for the dither offset. In the second and third panel from the top we show the relative throughput (i.e., integral under the Gaussian fit) and the FWHM of the seeing, respectively. The bottom panel presents the weight, which is the maximum flux of the Gaussian fit, and thus proportional to the throughput and the inverse seeing.

slightly shifted with regard to each other, and while finding the wavelength solution, we fit and correct for this offset. The combination of the slit edges and the 2D polynomial fit gives us the wavelength solution for each pixel in each original frame.

The last piece of information required to rectify the spectra is the relative offset of the frames. The dither stored in the header is used as an initial guess of the position of the target. Using this initial guess, we find the position of the slit star, which is used as the real offset. For this measurement, we first rectify the sky-subtracted spectrum of the brightest slit star to the reference coordinate system using the wavelength solution derived in the previous step in combination with the assigned dither positions. Next, we measure the position of the star in the rectified frames by fitting the profile with a Gaussian. In Figure 3 we show the y position (i.e., spatial position) of the slit star for all exposures of one example mask and filter (gn2_04, J). It is clear that there is a systematic and monotonic drift of ~0″2 (~1 pixel) per hour. This drift occurs in nearly all sequences and is on average about one pixel per hour. The strength and direction of the drift vary with field and air mass. We correct all dither positions for this drift.

For each spectrum in each science exposure we derive the transformations between the raw and reference frame using the drift-corrected dither positions and the wavelength solution. By combining all transformations in one step, we resample our data only once, thus avoiding further smoothing and noise correlations. Using these transformations, we rectify all sky-subtracted and sensitivity-corrected spectra to the reference coordinate system. Hence, this is the only step during which our data are resampled. We also resample the combined masks and set all pixels that are affected >5% by a bad pixel or cosmic ray to zero. We combine the resampled science masks with the resampled masks for the sky frame(s). We remove any additional sky from the science spectra by subtracting the median at each wavelength.

The slit star provides a seeing and throughput measurement for each science exposure. We use these measurements to determine the relative weight of the different frames. We take the maximum flux of the best-fit Gaussian to the slit star profile as the weight factor. By using the maximum, we optimize according to image quality and throughput, which both contribute to a higher S/N of the final 1D extracted spectrum. The throughput, seeing, and weight of each individual frame for one example mask are shown in the lower three panels of Figure 3.

Finally, we combine all rectified, sky-subtracted, and sensitivity-corrected frames according to their weights, while masking bad pixels and cosmic rays, as described by

$$\bar{n}_{x,y} = \frac{\sum_{i=1}^{N} w_i m_{x,y,i} n_{x,y,i}}{\sum_{i=1}^{N} w_i m_{x,y,i}} \tag{1}$$

with $n_{x,y,i}$ the number of counts of pixel (x, y) in the rectified, sky-subtracted, and sensitivity-corrected science frame i, $\bar{n}_{x,y}$ the weighted mean of the count level of all frames at pixel (x, y), w_i the weight of science frame i, $m_{x,y,i}$ the mask value (1: included; 0: excluded) at pixel (x, y) of science frame i, and N the number of science frames.

In order to construct a noise frame for each reduced science spectrum, we rectify the original raw science and corresponding (non-flat-fielded) sky frame as well. We make a noise frame for each individual science exposure by combining the counts of the rectified science and sky frames and adding the readout noise in quadrature. If there is one sky frame, we simply add the counts of the science and the sky frame and multiply the readout noise of an individual frame by $\sqrt{2}$. We use the following expression to derive $\sigma_{x,y,i}$, the noise at pixel (x, y) of individual science exposure i:

$$\sigma_{x,y,i} = \frac{\sqrt{Gs_{x,y,i} + Gs_{x,y,i\pm1} + 2R^2}}{G} \tag{2}$$

with $s_{x,y,i}$ the total number of counts of pixel (x, y) in the rectified, non-sky-subtracted science frame i, $s_{i\pm1,x,y}$ the number of counts in pixel (x, y) in either the previous $(s_{i-1,x,y})$ or next $(s_{i+1,x,y})$ science frame used as sky, G the gain, and R the readout noise.

In cases where the sky frame is constructed of two surrounding frames in an ABA′B′ dither sequence, the sky noise will go down by $\sqrt{2}$. As we take the average of two sky frames, the sky noise (in electrons) becomes $\sqrt{G(s_{x,y,i-1} + s_{x,y,i+1})/4}$. For the readout noise, we add in
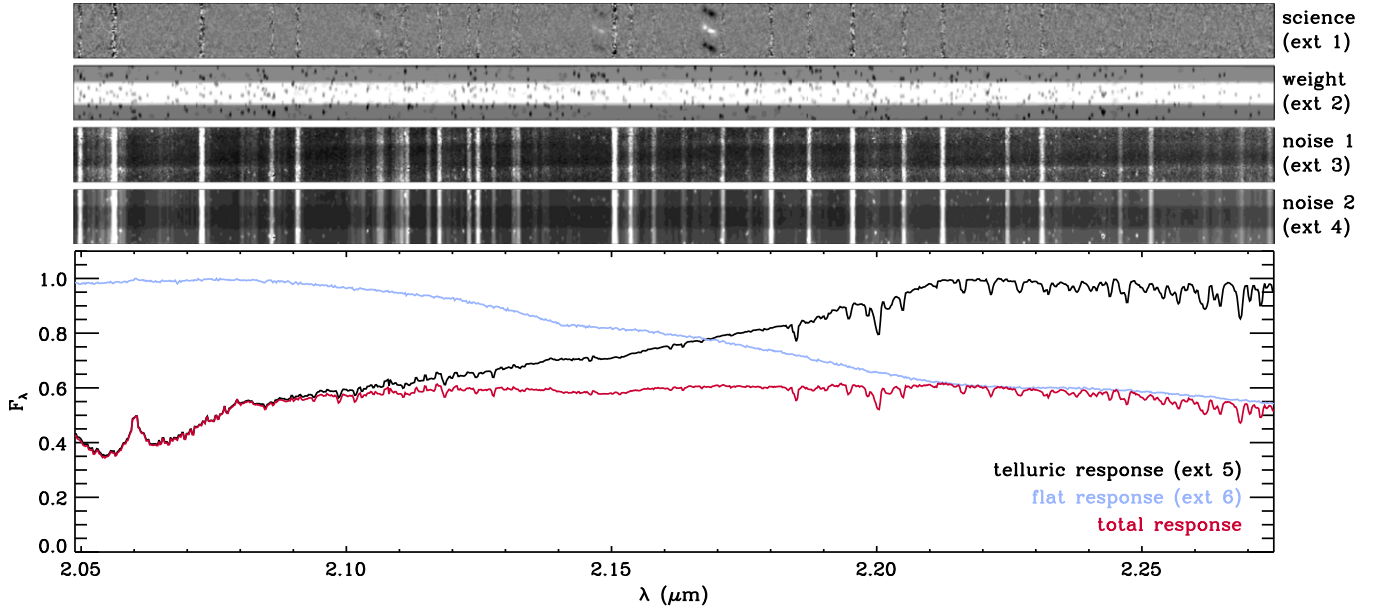
Figure 4. Overview of the MOSDEF 2D reduction pipeline data products for a $z \sim 3$ target in the K band. The top panel shows the 2D science frame, in which two [O III] lines and a faint Hβ line are visible in white. The negative emission lines in black are the result of using offset science frames as sky. The second panel from the top shows the weight frame with light pixels having larger weight. The gray horizontal bands indicate the regions that have been targeted by only half of the exposures. Dark spots indicate bad pixels or cosmic rays. The third panel from the top shows the noise frame constructed from variations between the separate science exposures. The fourth panel shows the noise frame constructed from the total number of counts, the gain, and the readout noise. We use this frame to derive our 1D error spectra. The bottom panel shows the 1D flat (blue) and telluric (black) response spectrum. Combined they form the total response spectrum (red). Only a fraction of the total K-band wavelength range is shown.

quadrature the readout noise of the science frame (R) and the combined readout noise of the sky frame $(R/\sqrt{2})$, which becomes $\sqrt{3/2}\,R$. By adding the background noise of the science frame, the background noise of the combined sky frame, and the total readout noise, we get the following expression:

$$\sigma_{x,y,i} = \frac{\sqrt{Gs_{x,y,i} + G\left(s_{x,y,i-1} + s_{x,y,i+1}\right)/4 + 3R^2/2}}{G} \quad (3)$$

We construct the final noise frame by adding the individual noise frames in quadrature, while taking into account their weights. For each individual pixel (x, y) we use the following expression:

$$\sigma_{x,y} = \frac{\sqrt{\sum_{i=1}^{N}(w_i m_{x,y,i}\sigma_{x,y,i})^2}}{\sum_{i=1}^{N} w_i m_{x,y,i}} \quad (4)$$

Finally, we correct the noise frame for the flat response, using the rectified flat frame.

We make a second noise frame, based on the variations between the rectified science exposures. This noise frame is based on resampled data, and thus we correct for random 2D resampling by multiplying the noise frame by a factor of 1.52.[20] We use the following expression:

$$\sigma_{x,y} = 1.52\sigma_{x,y,s} \frac{\sqrt{\sum_{i=1}^{N}(w_i m_{x,y,i})^2}}{\sum_{i=1}^{N} w_i m_{x,y,i}} \quad (5)$$

with $\sigma_{x,y,s}$ the sample standard deviation:

$$\sigma_{x,y,s} = \sqrt{\frac{\sum_{i=1}^{N} m_{x,y,i}\left(n_{x,y,i} - \bar{n}_{x,y}\right)^2}{N'_{x,y} - 1}} \quad (6)$$

with $N'_{x,y}$ the number of frames with nonzero weight at pixel (x, y).

Finally, we construct a weight map by combining the weights and rectified masks for each science frame:

$$W_{x,y} = \frac{\sum_{i=1}^{N} w_i m_{x,y,i}}{\sum_{i=1}^{N} w_i} \quad (7)$$

with $W_{x,y}$ the total weight at pixel (x, y).

The different reduction products are presented in Figure 4. We use the noise spectrum derived using Equations (2)–(4) for our 1D error spectrum (extension 4 in Figure 4). Nonetheless, in Section 3.4 we show that the different error spectra are consistent with each other.

3.2. Calibration

All spectra are calibrated for the relative response using telluric standards. During most nights, we observed telluric standards at similar air masses as the science observations. These spectra are reduced using the same method as that applied to the science masks. Similar to the science observations, we do not remove the flat response in the reduction. Thus, the overall flat response is canceled once the science spectra are divided by the telluric response spectrum. However, by keeping the response in the flat, we correct for the small difference in sensitivities as a function of wavelength among the different slits.
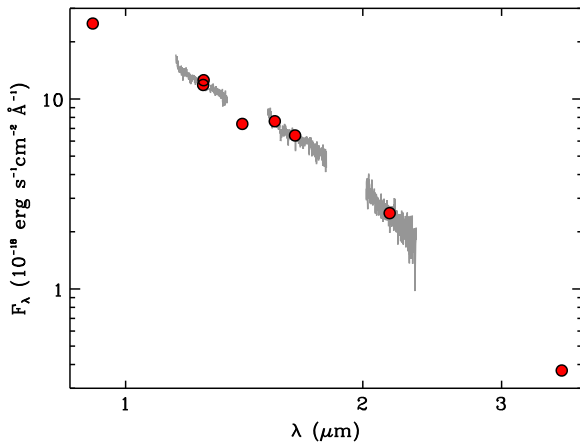
---

[20] This factor is derived by comparing the original noise of a frame to the noise after we randomly resample in both directions, while keeping the pixels the same size. We repeat this procedure 10,000 times and derive the average factor by which the noise has decreased.

Figure 5. Comparison of the MOSDEF J, H, and K spectra of a slit star with the photometry from 3D-HST ($H_{F160W} = 19.45$). The slit star spectra are scaled to match the 3D-HST photometry. All galaxies within the same mask are calibrated using this same normalization factor. A second correction is applied to take into account that slit losses depend on the spatial extent of the galaxies. This figure further illustrates the excellent agreement between the photometric and spectroscopic shapes.

We compare the observed telluric stellar spectra with the intrinsic spectra for the corresponding spectral type. The spectral types of the telluric standards range from B8 V to A1 V. These stars have Balmer and helium absorption lines, which may differ in line width or depth from the telluric standards we observed. Thus, in both the observed and the intrinsic spectra we interpolate over stellar absorption features. We derive a response spectrum by dividing the observed by the intrinsic stellar spectrum of the same spectral type. For the interpolated regions, we multiply the response spectrum by a theoretical sky absorption spectrum for the corresponding air mass.

To construct the response spectrum for a specific mask and filter, we combine multiple tellurics at similar air mass observed over different nights, to match the effective air mass of the final science frame. There are several reasons why we adopt this approach, instead of using only one response spectrum for a specific night. First, telluric standards are not available for all nights, and, if they are available, the air mass match is often not optimal. Second, some telluric spectra are noisy, which would increase the noise of our galaxy spectra. Third, the telluric spectra taken in 2012 and 2013 do not have full coverage in the H and K bands (see Section 2). Finally, we do not find a substantial difference in the atmospheric absorption features at a given air mass between different nights. When combining the response spectra of different nights, we take into account differences in the flat response - because a flat lamp change took place on 2014 February 13.

For the absolute flux calibration we make use of the slit star. First, we extract a 1D spectrum using the same optimal extraction method that we use for the galaxy spectra (see Section 3.6). We derive a scaling factor by comparing this slit star spectrum with the photometry in the 3D-HST photometric catalogs. Because most slit star spectra are only partially covered by any photometric filter, we do not integrate the spectra with the filter response curve of the closest 3D-HST photometric band. Instead, we fit the 3D-HST photometry and scale the spectrum to the fit. We only use the corresponding and surrounding filters to ensure that the fit perfectly matches the photometry, and we assume a simple blackbody shape. We calibrate all spectra within a mask using this normalization factor. The normalization factors, which include the slit-loss correction for a point source, are in the range $0.8 - 5.9 \times 10^{-17}$ erg cm^{-2} Å^{-1} cts^{-1}. In Figure 5 we show the scaled 1D spectrum of the slit star of mask gn2_06 in combination with the 3D-HST photometry used for the scaling.

3.3. Slit-loss Corrections

A crucial step in using the MOSDEF spectroscopy to calculate line flux ratios and absolute luminosities is to account for the loss of flux outside the slit apertures. As explained in the previous section, all spectra on a given mask for a given filter are scaled by a normalization factor computed by comparing the slit star spectrum with the 3D-HST photometry. This procedure accounts for both the conversion of counts to flux and the slit loss, assuming that the galaxies are unresolved point sources. However, most of the galaxies are in fact resolved based on an estimate of their sizes from the HST F160W images and the typical seeing of our observations.

Thus, we adopt the following procedure to better account for the loss of flux outside the slit aperture for each galaxy. First, we extract an F160W postage stamp of the galaxy from the CANDELS F160W imaging (Skelton et al. 2014) and use the SExtractor (Bertin & Arnouts 1996) detection segmentation map[21] to mask out all pixels in the postage stamp belonging to other nearby sources, retaining pixels that sample the background. The masked-out pixels are replaced by noise that is calculated from the average and standard deviation of the background pixel values. Second, we smooth the postage stamp with a Gaussian kernel with FHWM = $\sqrt{\text{FWHM}_{seeing}^2 - \text{FWHM}_{F160W}^2}$, where FWHM$_{seeing}$ is the seeing derived from the Gaussian fit to the profile of the slit star observed on the same mask and in the same filter (see Section 3.1) and FWHM$_{F160W}$ is the FWHM of the F160W PSF. Third, we fit the smoothed image of the galaxy with a 2D elliptical Gaussian that is allowed to rotate freely to obtain the best fit. Fourth, the modeled profile is rotated into the frame of reference of the slit, taking into account the P.A. of the slit. Fifth, the elliptical Gaussian is integrated within the slit boundaries to arrive at the fraction of light contained within the slit. Finally, each spectrum is multiplied by the ratio of the included fraction of light measured for the slit star (assuming a circular Gaussian) and that measured for the elliptical Gaussian. This last step corrects each galaxy spectrum for the additional light lost outside of the slit, relative to the slit star.

The effectiveness of this procedure is tested by first calculating the median fluxes from the best-fit SEDs of the continuum-detected galaxies (where the median is computed between wavelengths covered by our actual spectra) and then comparing these median SED-inferred fluxes with the median spectroscopic fluxes (see Figure 6). Taking into account the measurement errors, this comparison indicates that the uncertainties in flux calibration are ≈16%, with a bias of less than 18%. Similarly, for the line ratios spanning different filters (e.g., Hα/Hβ, [O III]/[O II]), we find a random uncertainty of 18% and a bias of less than 13%.

---

[21] The segmentation map indicates which pixels contain flux from objects and have nonzero values where objects are detected. Pixels without detections have a zero value.
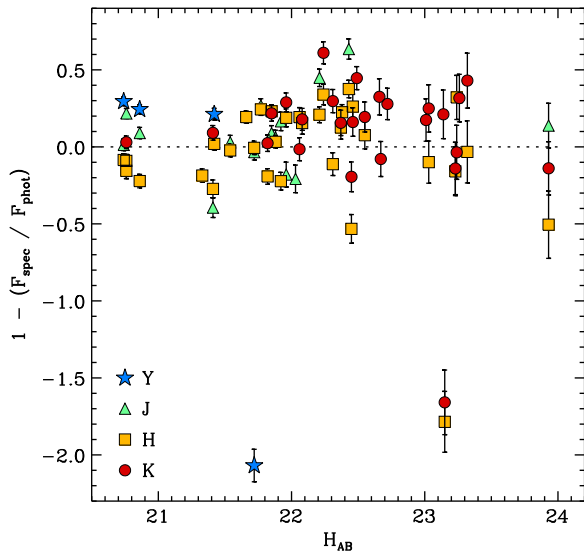
Figure 6. Comparison of the photometric to spectroscopic flux as a function of H_{F160W} magnitude for galaxies with continuum detections. All MOSDEF spectra are calibrated using a scaling factor derived by comparing the spectrum and photometry of the slit star, in combination with a slit-loss correction. Hence, the photometric fluxes of the galaxies are not used to calibrate the spectra, and thus a comparison with the spectroscopic fluxes gives an estimate of the uncertainty in the flux calibration. This comparison indicates that the uncertainties in flux calibration are $\approx 16\%$, with a bias of less than 18%.

We caution that the slit-loss corrections are based on rest-frame optical continuum emission, and thus the total emission-line fluxes as derived in Section 4 may be over- or underestimated, depending on whether the line emission is more or less concentrated than the continuum emission. One possible method to address this issue is to correct the line emission separately for slit losses using *HST* imaging in the rest-frame UV, which is more sensitive to star-forming regions. However, the use of bluer bands suffers from other complications, such as patchy dust attenuation, and thus it will not necessarily result in more robust slit-loss corrections.

3.4. Noise Properties

To quantify the significance of our results, it is crucial that we understand the noise properties of our observations. As described in Section 3.1, we construct two independent noise frames for each reduced mask. The first noise frame is derived from the number of counts, gain, and readout noise level of the detector (Equations (2)–(4) extension 4), and the second one is based on the variations between the rectified individual frames (Equations (5)–(6) extension 3). As both noise frames are derived using indirect methods, we use a third independent method, which is based solely on the reduced spectra, without using intermediate data products. For each of these three methods we make a 1D noise spectrum. For a fair comparison we only consider the wavelength range that is covered by all slits and masks for a specific filter (Y: 9700–10900 Å, J: 11700–13100 Å, H: 15400–17200 Å, K: 20400–22900 Å).

The third method is based on the variations of extracted 1D spectra in empty, yet fully exposed regions of the reduced 2D spectra. First, we take all reduced 2D spectra of a mask and we exclude all regions that are not fully exposed by removing the rows that have a normalized median weight of less than 0.92 (i.e., non-fully exposed regions). Thus, the gray and black rows in the weight panel of Figure 4 are not included. Second, we
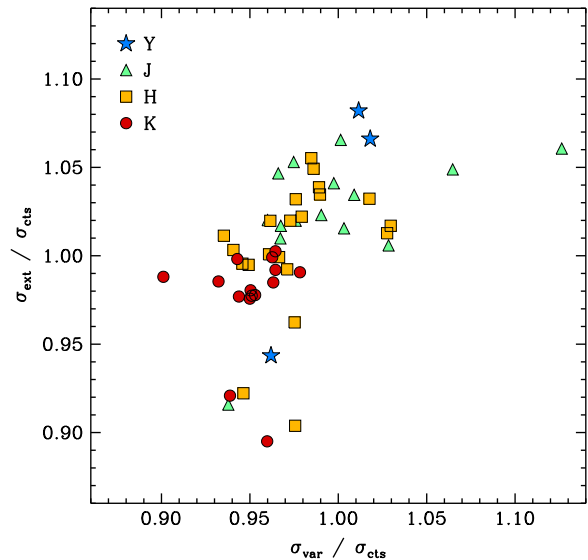

Figure 7. Comparison of three different noise measurements, as derived through independent methods. For all noise measurements, we determine the median noise level over the wavelength range covered by all spectra for a specific filter (Y: 9700–10900 Å, J: 11700–13100 Å, H: 15400–17200 Å, K: 20400–22900 Å). The x axis shows the ratio of the noise as derived from the frame-to-frame variations (σ_{var}) to the noise based on the total number of counts combined with the gain and readout noise (σ_{cts}). On the y axis we show the ratio of the noise as derived by extracting spectra in empty regions (σ_{ext}) to σ_{cts}. The mean of $\sigma_{ext}/\sigma_{cts}$ for all masks and filters is 1.00, and the mean of $\sigma_{var}/\sigma_{cts}$ is 0.97.

bin the 2D reduced spectra in the wavelength direction by five pixels to remove the effect of resampling in the 2D reduction. Third, we extract spectra in the empty regions (i.e., avoiding objects) using the same optimal extraction method as for our real spectra and a profile with an FWHM of 0″6, to represent typical seeing values for our observations. We extract as many independent empty spectra as possible across all slits on the mask. Each mask allows roughly 80 such empty apertures. Finally, we use the standard deviation at each wavelength as an estimate of the 1D noise spectrum.

To compare the results of this third method with the two different 2D noise spectra produced by the reduction procedure, we use the same "empty and fully exposed" regions. But first, similar to the reduced 2D science spectra, we bin the 2D noise spectra in the wavelength direction by five pixels as well, by taking the square root of the summed variance. Next, we (optimally) extract a 1D noise spectrum from the binned noise frame for each empty region (corresponding to the same regions used to extract the empty spectra in the science spectra), assuming the same profile. Finally, we take the average of the 1D noise spectra for all empty regions to construct the mean 1D noise spectrum. Using this method, we make a 1D noise spectrum for both of the noise frames in extensions 3 and 4. To compare the different 1D noise spectra, we assess their ratio as a function of wavelength. Because the ratios show no trend with wavelength, we derive a median value for the ratios for each mask over the wavelength regions covered by all spectra (defined in the first paragraph of this section). The results of this test are presented in Figure 7.

Figure 7 illustrates that the three different noise measurements agree very well. The median ratio between the empty

aperture and sky noise (extension 4, Equations (2)–(4)) method for all different masks and filters is 1.0. The median ratio between the frame variation (extension 3, Equations (5)–(6)) and the sky noise method is 0.97. These ratios are robust against different aperture sizes. There is a slight difference between the different filters, with the K band yielding a relatively lower noise level for the empty aperture method compared to the other methods. The exact reason for this difference is not well understood. Hereafter, we use the sky and readout noise (extension 4) as the noise spectra in our analysis.

3.5. Assessment

Our observational and reduction procedures contain several steps that differ from the conventional procedure to obtain and reduce near-IR spectroscopic data. Here, we assess the improvement by these steps, by turning off the corresponding features in the reduction procedure. We show that the improvement due to an individual step is generally only a few percent. However, the inclusion of all steps together may lead to an improvement of up to 25% in the total S/N of the 1D reduced spectra.

The first step we assess is the dither sequence. We use an ABA′B′ dither sequence, with a distance between A and B of $2\rlap{.}''7$, and a distance between A and A′ (and B and B′) of $0\rlap{.}''3$. This observing sequence has several advantages over the commonly used ABBA or ABAB dither pattern. The first advantage is that different parts of the detector are used, and thus bad pixels are spread out over multiple exposures. The second advantage is that we can use two surrounding frames as sky, which lowers the noise in the sky frame by a factor of $\sqrt{1/2}$. In the appendix we show that the reduction of noise in the sky frame by a factor of $\sqrt{1/2}$ leads to a reduction of the noise in the sky-subtracted science frame by a factor of $\sqrt{3/4}$, compared to using only one sky frame. The ABAB dither sequence also allows the use of two sky frames and thus a lower noise level in an individual sky-subtracted frame. However, when adding the sky-subtracted frames, this dither sequence is effectively similar to an ABBA dither sequence with one sky frame (see Appendix). For the final 1D spectrum, the improvement in S/N is optimal if the distance between A and A′ is larger than the extraction aperture.

To assess the S/N improvement due to the dither sequence in combination with the multiple sky frames, we reduced several masks, while only using one of the surrounding frames as sky (A-B, B-A, A′-B′, B′-A′, and so on). When considering the S/N improvement, we use the noise spectra based on the empty aperture extractions because this is the most direct and empirical method of determining the noise. The noise frame based on the count level (extension 4) will by definition give an improvement of $\sim\sqrt{3/4}$ (the difference between Equations (2) and (3)) and thus cannot be used as an independent test. The noise spectrum based on the frame-to-frame variations (extension 3) assumes that the extraction aperture is smaller than the offset between A and A′, and thus neither can be used. In Figure 8 we compare the ratio in S/N between the reduction with a single sky frame (diamonds) and the MOSDEF reduction as a function of seeing. As expected based on the small offset between A and A′, the improvement is less than the theoretical value.

Another improvement in our reduction scheme, facilitated by the multiobject mode, is the simultaneous monitoring of a
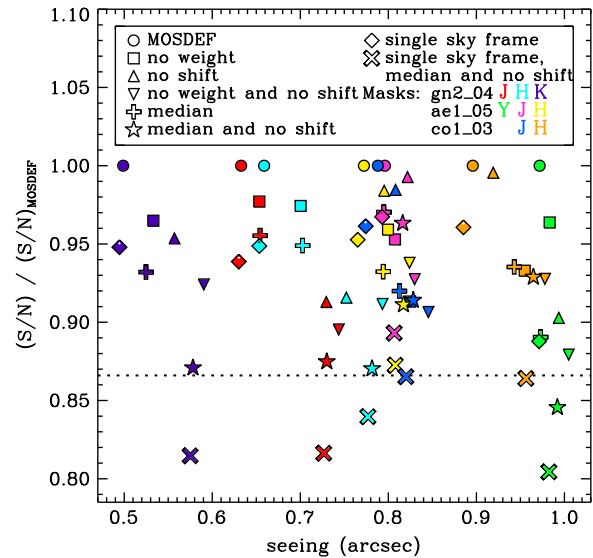

Figure 8. S/N for alternate reductions, compared to the S/N of the official MOSDEF reduction (circle) vs. the seeing. We explore the improvement that is due to weighting individual frames (square), applying a drift correction (triangle), and correcting for both effects (upside-down triangle). We also include a median combine (plus) and a median combine without correcting for the drift (star). Finally, we assess the improvement that is due to the inclusion of two instead of one sky frame (diamond). The dotted line indicates the theoretical difference ($\sqrt{3/4}$) between using one or two sky frames. Compared to a median combine with no drift correction and one sky frame (cross), our reduction increases the S/N by up to $\sim$25% ((1.00–0.80)/0.80).

relatively bright star in one of the slits. Using this slit star we weight individual frames, trace the drift, and calibrate our spectra. In Figure 8 we show the S/N when reducing the data without weighting the individual frames (squares) or correcting for the drift (triangles), compared to our standard MOSDEF reduction pipeline. We also test the use of a median instead of a mean (plus signs). We use the same mask and noise frame as for the dither test, so we can assess the total effect of all improvements.

For all cases, we find that the MOSDEF reduction results in the highest S/N. For most masks, the lowest S/N is obtained for a median combine without a drift correction (stars). Compared to this reduction, the S/N of the MOSDEF reduction is up to $\sim$18% higher ((1.00–0.85)/0.85 = 0.18). The combined effect of all different procedures increases the S/N by up to 25% ((1.00–0.80)/0.80 = 0.25), compared to a single sky frame, no shift, and a median combine reduction (crosses). Increasing the exposure time by 50% would result in the same S/N increase.

3.6. Extraction of 1D Spectra

The 1D spectra are extracted by hand using custom IDL software (see W. Freeman et al. 2015, in preparation, for a full description).[22] The extraction program works with output from the custom MOSDEF 2D reduction pipeline discussed in the previous sections. Both optimally weighted and unweighted spectra are extracted for each object. The optimal extraction algorithm is based on Horne (1986) and is extended to be able to extract fractions of pixels.

First, the extraction program uses the expected y position of an object, as given by the MAGMA output files, to draw a line that clearly marks the position of the primary object in the 2D

---

[22] https://github.com/billfreeman44/bmep

spectra. However, because of the drift correction, the expected position is slightly shifted compared to the real position.[23] We use the position of the slit star in the same mask and filter to correct the expected position. Using the line at the expected position, we unambiguously identify the primary object.

Next, the spatial profile of the object is determined by summing only those columns of the 2D spectra with high S/N in either the continuum or emission lines. This method provides clean weighting profiles for the optimal extraction because columns with little or no signal are excluded. We fit a Gaussian function to the profile to determine the weighting profile, center, and width of each object. For the extraction aperture, we take twice the FWHM of the Gaussian function. Finally, 1D spectra are extracted with and without optimal weighting. We apply this procedure to each object and each filter, separately. Serendipitous objects are also extracted using the same method, and 89% of them are identified as objects in the 3D-HST catalog v4.0 (Skelton et al. 2014).

In cases where an object has no obvious emission lines or continuum in the 2D spectrum, a "blind" extraction is performed. For objects with no signal in any band, the blind extraction uses the expected position of the object, as derived from the MAGMA output file and the slit star position, and uses the same extraction width as the width of the slit star in each filter. For objects with signal in one or more bands, the blind extraction uses the average extraction widths and centers from filters in which a signal was detected, corrected for seeing and offset differences as derived from the slit star profiles and positions.

4. ANALYSIS

In this section we describe the procedure to measure emission-line fluxes and redshifts, present the sensitivities of the line and continuum emission, and outline the procedure to derive stellar population properties from multiwavelength photometry in combination with the MOSFIRE redshifts. We also assess for which galaxies we successfully obtain a spectroscopic redshift and how the targeted and spectroscopically confirmed galaxy samples compare to an H-band-limited galaxy sample at the same redshift.

4.1. Emission Line Measurements and Sensitivities

We use a Monte Carlo method to measure emission-line fluxes and errors by perturbing the spectrum of each object by its error spectrum. For each object, we measure an initial redshift and line width by fitting a Gaussian to the highest S/N emission line, which in most cases is either the $H\alpha$ or [O III] $\lambda5008$ line. The initial redshift and FWHM are then used to fit all of the other lines of interest. In the fitting, we allow the observed wavelengths of the lines (as predicted from the initial redshift) to vary within $\pm 2 \times (1 + z)$ Å, and we allow the FWHM to vary within $\approx \pm 0.5$ Å in the observed frame, excluding values that are lower than the instrumental resolution. The [O II] doublet is fit with a double Gaussian function, and the $H\alpha$ and [N II] doublet is fit with three Gaussians. In addition, for all lines we allow for a linear continuum fit under the Gaussian. We repeat this procedure using 1,000 different realizations of the spectra and calculate the average line fluxes

and dispersions from these realizations. For each line, we obtain an estimate of the slope and intercept of the continuum under the line, the observed wavelength, the line flux, and the FWHM.

To more reliably measure fluxes for lines that deviate significantly from a Gaussian shape, we also simply integrate the flux under each line using fixed-wavelength windows (f_{window}). This second flux measurement is adopted if (1) the Gaussian model fit to the line deviates from the data by more than 2σ (as determined from the error spectrum) in any given pixel within $\pm 3\sigma_w$ (i.e., line width) of the line center and (2) the absolute value of the difference between f_{window} and the fitted flux is more than three times the fitted flux error: i.e., $|f_{window} - f_{fitted}| > 3\,\sigma_{fitted}$. The fluxes of the Balmer $H\alpha$ and $H\beta$ emission lines are corrected for underlying Balmer absorption using the best-fit stellar population model, as derived in Section 4.5.

In Figure 9 we show the S/N of the emission lines [O II], $H\beta$, [O III], $H\alpha$, [N II], and [S II] versus the flux of the lines. Because the spectra are corrected for slit losses, the line flux shown here represents the total line flux of the galaxies, assuming that the line flux originates from the same region as the stellar continuum as traced by the F160W images. We only include galaxies for which the redshift is directly measured from the MOSDEF spectra from either $H\alpha$ or [O III], and we exclude serendipitous detections.

The [O III] and $H\alpha$ lines are the strongest emission lines in our spectra. However, even fainter lines are significantly detected in most spectra. Within 2 hr we obtain a 5σ line detection for a typical flux of $\sim 1.5 \times 10^{-17}$ erg s^{-1} cm^{-2}. The line-flux sensitivity is slightly deeper in the H band, as expected from the MOSFIRE specifications and sky background level, though the sensitivity difference between filters for our full set of emission-line measurements is masked by the variation in observing conditions. In the most optimistic case, when avoiding sky lines and bad weather conditions, our 5σ depth within 2 hr is $\sim 6.1 \times 10^{-18}$ erg s^{-1}cm^{-2} and 7.4×10^{-18} erg s^{-1}cm^{-2} for H and K, respectively.

For a 5σ line detection within 1 hr, Steidel et al. (2014) find a typical line flux of 3.5×10^{-18} and 4.5–14×10^{-18} erg s^{-1} cm^{-2} in H and K, respectively. In contrast to Steidel et al. (2014), our fluxes are all corrected for slit losses. The mean slit-loss corrections are a factor of 1.69, 1.66, 1.62, and 1.54 for Y, J, H, and K, respectively. Taking into account the integration time difference and the slit-loss correction, we find a difference of a factor of 1.5 between our optimistic 5σ depth and the 5σ depth found by Steidel et al. (2014) for the H band. In addition, differences in the methods to construct the noise frames, extract the spectra, and measure the emission-line fluxes, as well as in the targeted galaxies (e.g., line widths) and weather conditions, may further contribute to differences in depth.

We compare the emission-line measurements from MOSDEF with those from 3D-HST in Figure 10. Because the resolution of 3D-HST is not high enough to deblend close emission lines, we combine the flux measurements of the unblended lines in MOSDEF as well, for a fair comparison. In Figure 10 we only show primary targets and lines that are detected at 3σ in both data sets. Here [O III] is the sum of the 4960 and 5008 Å lines, and for $H\alpha$+[N II], we add the flux of the $H\alpha$ line (corrected for Balmer absorption) and the two [N II] lines at 6550 Å and 6585 Å.

---

[23] In rare cases, an offset was skipped during the observations, resulting in an even larger difference between the expected and measured positions of the spectrum.
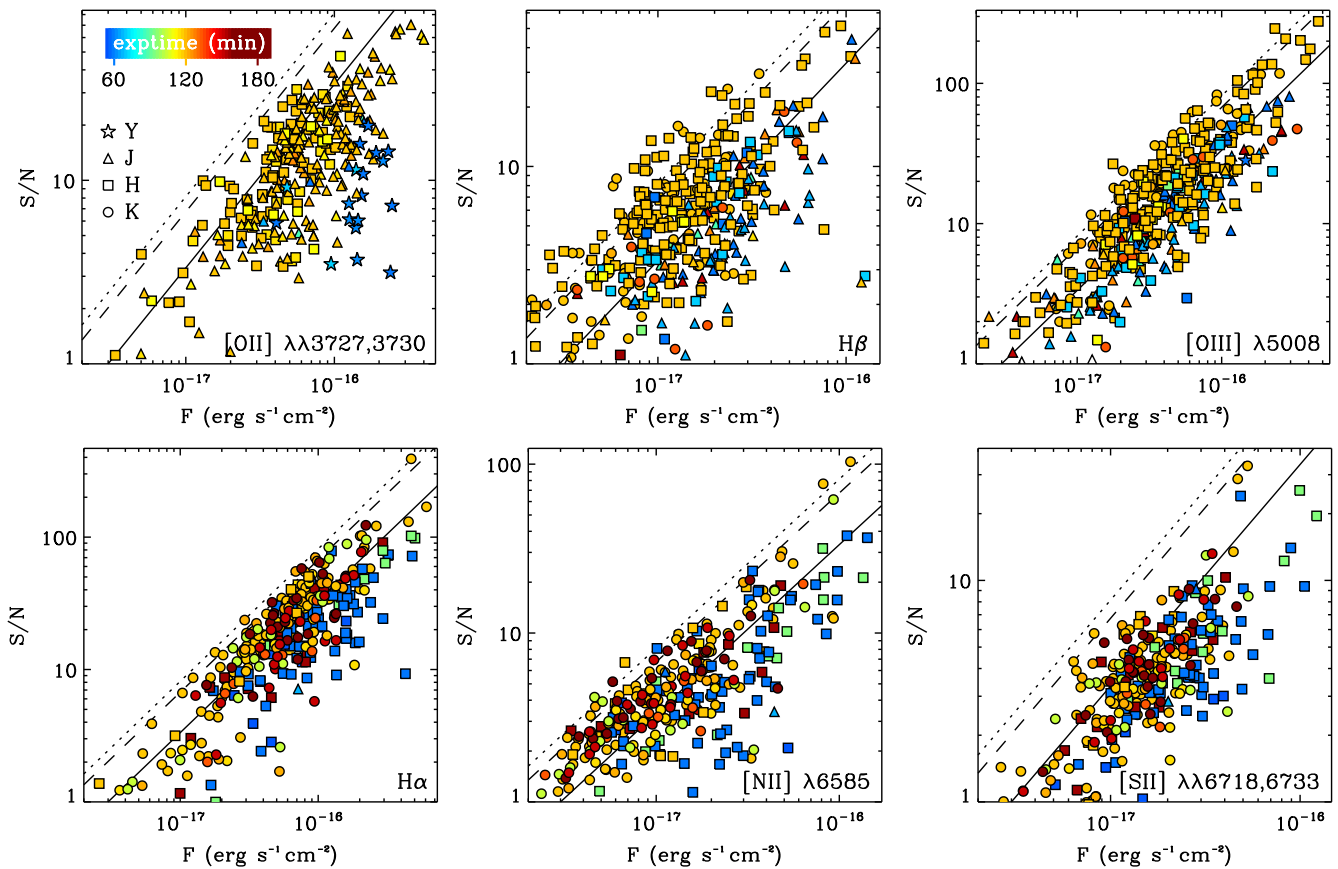
Figure 9. S/N of emission lines [O II], Hβ, [O III], Hα, [N II], and [S II] vs. the total flux (corrected for slit losses) of the line. In this figure, Hα and Hβ are uncorrected for the underlying absorption. The features are measured in the optimally extracted 1D spectra, and serendipitous detections are excluded. The color coding reflects the integration time, and the symbol indicates the filter in which the line is detected. The black solid line shows our typical emission-line depth for a 2 hr exposure. The black dotted and dashed lines represent our most optimistic depths (i.e., avoiding sky lines and bad weather conditions) in 2 hr for H and K, respectively. These depths are calculated using the Hα emission lines.
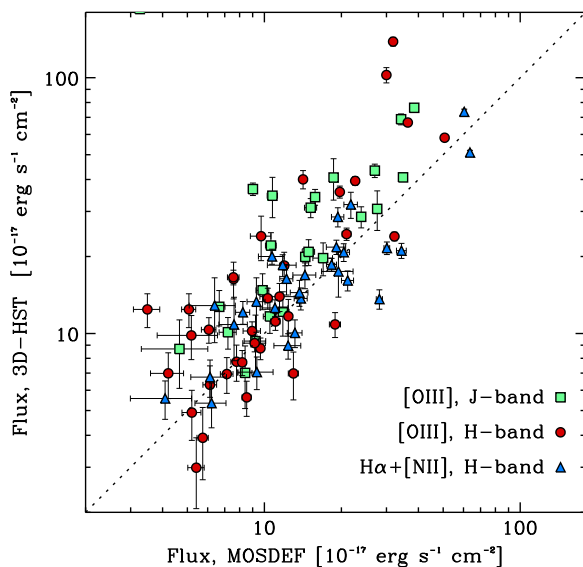
Figure 10. Comparison of emission-line fluxes as measured from MOSDEF and 3D-HST. We consider lines with an S/N > 3 in both the MOSDEF and 3D-HST spectra. Because of the lower spectral resolution of the 3D-HST grism spectra, we combine Hα and the two [N II] lines and the two [O III] lines for MOSDEF. The flux measurements for both surveys are corrected to the total flux by scaling the spectra to the 3D-HST photometry.

The two data sets agree reasonably well, with a median offset and scatter (σ_{NMAD}) in $1 - F_{MOSDEF}/F_{3D-HST}$ of ∼13% and 35%, respectively. The random difference is larger than expected based on the uncertainties in the individual MOSDEF and 3D-HST line measurements. This is not surprising because both uncertainties do not take into account errors introduced by the absolute flux calibration. In Section 3.3 we find a random uncertainty of 18% and a bias of less than 13% for the MOSDEF absolute flux calibration. Furthermore, these values do not include additional errors on the slit-loss corrections because the line emission may not follow the continuum emission. The 3D-HST spectra are also scaled using the photometry. This procedure may introduce additional (systematic) uncertainties in the 3D-*HST* emission-line fluxes as well.

For galaxies for which the weighting profile is determined from line emission *and* for which the line and continuum emissions originate from different regions in the galaxy, we caution that the spectra will be biased toward the line-emitting regions. Because the continuum emission will be downweighted for these galaxies, the emission-line equivalent widths may be overestimated. To check whether the emission-line fluxes may have been affected by the optimal extraction, we have repeated our line-fitting procedure for the boxcar extractions. We find no systematic offset in emission-line fluxes between the two extractions. Finally, emission-line measurements using the
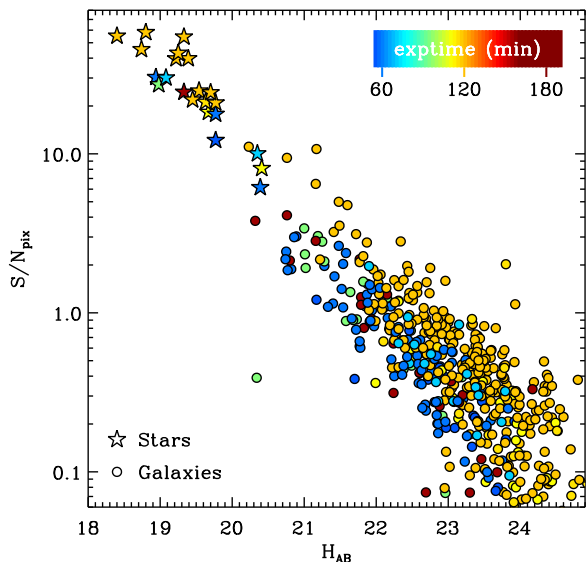
Figure 11. Median S/N per pixel in the optimally extracted H-band spectra vs. the total H-band magnitude for all observed stars (stars) and galaxies (circles). The color coding reflects the integration time. Serendipitous detections are not included in this figure. This figure does include bad-weather masks, explaining the low S/N for galaxies with long integration times.

boxcar extractions do not give a better agreement with the 3D-HST line fluxes, thus suggesting that no significant bias has been introduced by the optimal extraction method.

4.2. Continuum Emission Sensitivities

In Figure 11 we show the S/N per pixel of the continuum emission in the optimally extracted H-band spectra as a function of the total F160W (H_{AB}) magnitude. We take the median S/N level in the wavelength interval covered by all spectra, given in Section 3.4. We show both the measurements for the galaxies and the slit stars of all masks. The symbols are color coded by the total exposure time. For galaxies at $z \sim 2.3$, one pixel in the H band corresponds to 0.44 Å in the rest frame, and thus the S/N per rest-frame Å is ~1.5 times larger.

There is a large range in sensitivities among the different continuum detections for the same integration time and F160W magnitude. This scatter reflects the range in weather conditions and the difference in structural properties of the galaxies. For example, for more extended galaxies or for larger values of the seeing, both the extraction aperture and the slit losses are larger, resulting in lower values for the S/N.

To measure the S/N in each filter and directly compare the depth and seeing conditions of the different masks, we calculate the 3σ depth (per pixel) for a point source directly from the spectra. For this measurement, we optimally extract a noise spectrum using the profile of the slit star on several empty areas on the detector. Next, we take the median noise level over the wavelength region targeted by all spectra (see Section 3.4). We multiply this value by a factor of three to derive the 3σ depth in F_λ. We convert this depth to the AB magnitude, using the effective wavelength of the corresponding filter. Because these depths are derived from the calibrated data, both the AB magnitude and the F_λ value are "total," thus corrected for slit losses.

Figure 12 presents an overview of the depth for all 21 masks as a function of the effective seeing of the reduced spectra.

Each panel represents a different filter, and each symbol represents one mask for a specific filter. The symbols are color coded by integration time. The sensitivities in Figure 12 are only valid for faint point sources. The noise level increases, and thus the depth decreases, for extended sources because of larger slit losses and a larger extraction aperture. For very bright sources, the depth will also decrease because the noise is not merely determined by the background level, and the source itself contributes to the noise level as well.

Figure 12 also shows the median 3σ depth given by the official MOSFIRE exposure time calculator (ETC, by G. Rudie) using the same wavelength region. We show the ETC results for a range in seeing and two exposure times (1 and 2 hr). The ETC does not account for slit losses, and therefore as input magnitude we have to give the magnitude of the flux that falls in the extraction aperture. Thus, we first convert the total magnitude to the extraction aperture magnitude. For the extraction aperture we take 0″7 (slit width) times twice the FWHM of the effective seeing (see Section 3.6). We also correct the ETC S/N for an optimal extraction by dividing by a factor of 0.81. We derive this factor by comparing the S/N of spectra extracted using an optimal extraction and a boxcar extraction with the same extraction aperture.

Figure 12 shows that the exposure time calculator is on average optimistic by a factor of about two, though two out of 21 masks in the H band are consistent with the theoretical expectations for their seeing (co2_03 and co3_04). Non-optimal or variable weather conditions may contribute to the difference between the expected and measured performance.

4.3. Absorption Line Redshifts

For galaxies with strong continuum emission but no line emission, we derive spectroscopic redshifts from the absorption lines. There are 14 targets with an $S/N_{pix} > 3$ in the H band (see Figure 11). Eight of 14 targets have detected emission lines. Most of these galaxies show clear absorption lines in their spectrum as well. The six remaining galaxies all have quiescent SEDs (as identified using their rest-frame $U - V$ and $V - J$ color; see Section 4.6), explaining the lack of detected emission lines.

In order to determine a spectroscopic redshift, we fit the spectra (in combination with the photometry) of the six targets without emission lines by stellar population models, using the fitting code FAST (Kriek et al. 2009b). For three out of six spectra, the fitting yields robust spectroscopic redshifts, and for one spectrum the spectroscopic redshift is less robust. One spectrum has no coverage in the 4000 Å break region, in which nearly all strong absorption lines are expected. Thus, for this galaxy no robust redshift is obtained. The remaining galaxy is too noisy to yield a spectroscopic redshift. Two of the three spectra for which we measure a robust redshift target the same galaxy (COSMOS-11982). The spectrum in mask co2_03 has an S/N of 9.4 per pixel in the H band, and the spectrum in mask co3_01 has an S/N of 4.1. By fitting the spectra independently, we find the same spectroscopic redshift of $z = 2.089$.

4.4. Spectroscopic Success Rate

An important factor for the overall success rate of our survey is the fraction of galaxies for which we measure a robust spectroscopic redshift. For 462 out of 591 primary MOSDEF galaxies, we securely identify and measure emission lines in
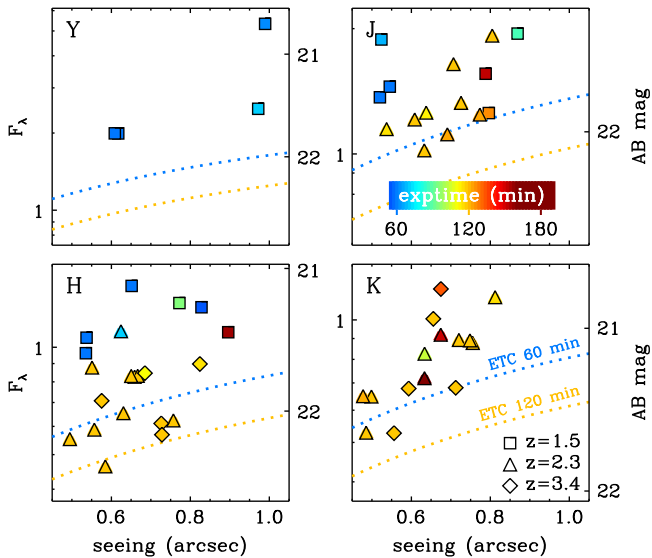
Figure 12. Total flux F_λ (in 10^{-18} erg s^{-1} cm^{-2} Å^{-1}) or AB magnitude of an artificial object for which we obtain an S/N of three per spectral pixel, as a function of seeing. Each data point represents a different mask and filter, the colors reflect the exposure time, and the symbols indicate the targeted redshift of the mask. The depths are derived from the optimally extracted 1D spectra in empty parts of the detector using the slit star profile and thus are only valid for faint point sources. For a fair comparison, we take the median noise level in the wavelength regime covered by all spectra. The 3σ depths as derived by the exposure time calculator (ETC) for 60 and 120 minutes using the same method and wavelength range are presented by the dashed blue and orange lines, respectively.

Table 2
Success Rate of Targeted Galaxies

Mask	$N_{\rm targeted}$			$N_{\rm confirmed}$			$F^{\rm a}$	$N_{\rm ser}$
	$z_{\rm low}$	$z_{\rm mid}$	$z_{\rm high}$	$z_{\rm low}$	$z_{\rm mid}$	$z_{\rm high}$	%	
ae1_01	25	3	0	20	3	0	82	4
ae1_05	25	2	1	15	2	0	61	3
co1_03	26	2	1	16	2	0	62	0
co1_05	20	5	1	10	2	0	46	3
gn1_04	24	3	0	17	1	0	67	2
ud1_01	32	1	0	29	1	0	91	0
ae2_03	3	24	0	4	21	0	93	4
ae2_04	0	27	2	1	25	1	93	2
ae2_05	1	26	2	0	21	2	79	2
co2_01	2	29	0	1	25	0	84	5
co2_03	1	24	0	0	21	0	84	7
co2_04	2	25	0	1	22	0	85	4
gn2_04	1	24	2	1	19	1	78	2
gn2_05	0	22	6	0	21	5	93	4
gn2_06	1	24	3	2	17	2	75	1
gs2_01	0	26	0	0	21	0	81	0
ae3_04	3	2	26	2	2	22	84	0
co3_01	0	8	21	0	9	11	69	3
co3_04	0	3	26	1	3	18	76	0
co3_05	3	2	25	2	2	24	93	6
gn3_06	1	2	21	0	2	17	79	3
Total	170	284	137	122	242	103	79	55

Note. ae1_05, co1_03, and co1_05 are bad-weather masks.
$^{\rm a}$ Fraction of targeted galaxies for which we measure a robust spectroscopic redshift.

the 1D extracted spectra. In cases for which only one emission line is significantly detected, the spectroscopic red-shift is classified as robust if it is consistent with the photometric redshift within the typical photometric redshift uncertainty. There are three additional spectra for which we securely identify a redshift from multiple absorption lines. Thus, our spectroscopic success rate is 79% (465 out of 591). Thirty-one of the 465 galaxies have been observed and confirmed in two masks, and thus the number of unique galaxies with robust spectroscopic redshifts is 434.

Out of the 591 primary galaxies, 68 host an AGN, based on either their IRAC colors or X-ray luminosity (Coil et al. 2014). Thus, on average we target 3.2 AGNs per mask. This number does not include AGNs that are identified based on just their optical spectra. The spectroscopic success rate for AGNs is 75%. Three of the 51 confirmed galaxies hosting an AGN have been observed twice.

Table 2 gives an overview of the number of galaxies targeted per redshift regime for each mask and the number of galaxies for each redshift regime for which we measure a robust redshift. Each mask has a few fillers from the other redshift intervals. For nearly all galaxies, the prior redshifts fall in the targeted redshift intervals.[24] However, the MOSDEF redshifts are in some cases outside the redshift intervals. Thus, when giving the number of confirmed galaxies, we use broader redshift intervals (low: $z \leqslant 1.9$, middle: $1.9 < z \leqslant 2.75$, high: $z > 2.75$) in Table 2. For each mask we give the spectroscopic success rate, which is the ratio of all confirmed to all targeted galaxies. The three bad-weather masks have a lower success rate, with an average of 55%. If we do not include the bad-weather masks, our spectroscopic success rate is 82%.

There are 20 additional galaxies for which we detect emission or absorption lines, but the spectroscopic redshifts are inconclusive because of low S/N or because the multiple emission lines yield inconsistent redshifts. In addition, we have 55 robust redshifts for serendipitous detections. The left panel of Figure 13 shows the redshift distributions of the prior, robust, serendipitous and nonrobust redshifts. Most serendipitous detections fall in or near the targeted redshift ranges. This is not surprising because we are less sensitive to picking up features in between the atmospheric windows (see Figure 1). There are several serendipitous detections, though, that have lower redshifts.

In the middle and right panels of Figure 13 we compare robust MOSDEF redshifts (of primary targets only) with the prior redshifts used for target selection. The prior redshifts are a combination of spectroscopic redshifts from primarily optical spectroscopic surveys (see Section 2.1), 3D-HST grism redshifts (including and excluding emission lines), and photometric redshifts as derived from the 3D-HST photometric catalogs using EAzY. For the majority of galaxies with prior spectroscopic redshifts or with emission lines in the grism spectra, we confirm the redshift with a normalized median absolute deviation ($\sigma_{\rm NMAD}$, Brammer et al. 2008) of 0.0012 and 0.0016, respectively. For most galaxies with photometric or grism redshifts without detected emission lines, the MOSDEF redshifts are close to the prior redshifts with a $\sigma_{\rm NMAD}$ of 0.30 and 0.18, respectively. There are 16 galaxies that scatter from one to the other redshift window. Interestingly, nearly all of the catastrophic failures are galaxies with prior spectroscopic redshifts.

---

[24] Because of catalog updates, a few of the target redshifts were scattered outside the targeted redshift intervals after the galaxies were observed with MOSFIRE.
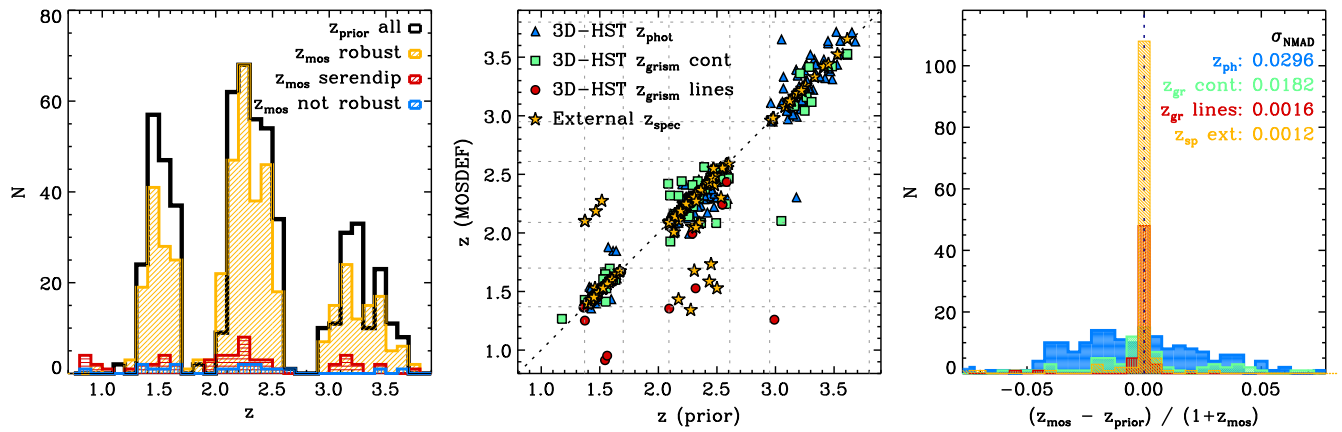
Figure 13. Left: MOSDEF redshift distribution compared to the prior redshift distribution used for our target selection (black histogram). The MOSDEF redshift distribution is divided into robust redshifts (yellow histogram), inconclusive redshifts (blue histogram), and robust redshifts derived for serendipitous detections (red histogram). The latter galaxies are not included in the black histogram. Middle: Comparison of MOSDEF and prior redshifts for primary targets with robust MOSDEF redshifts. The prior redshifts consists of spectroscopic redshifts when available (yellow stars), 3D-HST grism redshifts, or 3D-HST photometric redshifts when no grism spectrum is available (blue triangles). Grism redshifts are divided between those that are based on emission lines (red circles) and those for which only continuum emission is detected (green squares). The gray dotted lines indicate the target redshift intervals. Right: distribution of the difference in prior and MOSDEF redshifts for the four prior redshift classes, with the colors of the histograms corresponding to the colors of the symbols in the middle panel. The normalized median absolute deviation between the prior and MOSDEF redshifts are given for each prior redshift class.

For 36% of the confirmed MOSDEF galaxies, we had a spectroscopic redshift (including grism emission-line redshifts) prior to the survey. This fraction does not include galaxies with incorrect prior spectroscopic redshift. Thus, for 64% of the targets, only photometric redshifts, grism continuum redshifts, or incorrect spectroscopic redshifts were previously available.

4.5. Stellar Population Properties

For all targeted galaxies as well as galaxies in the parent catalogs, we derive stellar population properties by comparing the photometric SEDs with stellar population synthesis (SPS) models. The parent catalogs are the trimmed versions of the 3D-HST catalogs by Skelton et al. (2014), created by imposing the redshift and magnitude criteria for each redshift interval. We use the stellar population fitting code FAST (Kriek et al. 2009b), in combination with the flexible SPS models by Conroy et al. (2009). We assume a delayed exponentially declining star formation history of the form SFR $\propto t \exp(-t/\tau)$, with t the time since the onset of star formation, and τ the characteristic star formation timescale. The age is allowed to vary in the range $7.6 < \log(t \, \mathrm{yr}^{-1}) < 10.1$ in steps of $\Delta(\log(t \, \mathrm{yr}^{-1})) = 0.1$, but it cannot exceed the age of the universe at a given redshift. The star formation timescale τ can vary in the range $8.0 < \log(\tau \, \mathrm{yr}^{-1}) < 10.0$ in steps of $\Delta(\log(\tau \, \mathrm{yr}^{-1})) = 0.2$. We furthermore assume a Chabrier (2003) stellar initial mass function (IMF) and the Calzetti et al. (2000) dust reddening curve. Spectroscopic redshifts from MOSDEF are used when available. For galaxies without MOSDEF redshifts, we use the prior redshift information.

We include a template error function to account for template mismatch in less-constrained wavelength regions of the spectrum (Brammer et al. 2008). For example, the poorly understood, thermally pulsing asymptotic giant branch phase results in large uncertainties in the rest-frame near-IR part of the spectrum, and thus the wavelength range has a lower weight in the fit (e.g., Conroy et al. 2009; Kriek et al. 2010). The 1σ confidence intervals are derived using Monte Carlo simulations, by perturbing the photometry using the photometric

errors (corrected using the template error function). Next, we determine the χ^2 level that encloses 68% of the simulations. We take the minimum and maximum values allowed within this χ^2 level as the confidence intervals on all other properties (see Kriek et al. 2009b for a more detailed description). Whereas our default stellar population parameters are derived using the method above, other MOSDEF papers may use different methods (Reddy et al. 2015, Coil et al. 2015).

In addition to photometric SFRs, we also determine SFRs based on the Hα and Hβ emission lines. First, we derive a Balmer decrement from the ratio of Hα to Hβ. Both Hα and Hβ are corrected for the underlying Balmer absorption using the best-fit stellar population model. By comparing this ratio to the intrinsic ratio of Hα/H$\beta = 2.86$ for H II regions (Osterbrock 1989) and assuming the Calzetti et al. (2000) attenuation curve, we derive the reddening $E(B-V)$ and accordingly correct the Hα luminosity. Finally, we convert the Hα luminosity into an SFR using the relation by Kennicutt (1998), adjusted for a Chabrier (2003) IMF (see Reddy et al. 2015 for a more detailed description). In Figure 14 we show the SFRs and stellar masses for the $z \sim 1.5$ and $z \sim 2.3$ MOSDEF galaxy samples. This figure illustrates that our confirmed galaxies have stellar masses in the range 10^9–$10^{11.5} \, M_\odot$ and SFRs in the range 10^0–$10^3 \, M_\odot \, \mathrm{yr}^{-1}$.

In Figure 15 we show MOSDEF spectra, photometric SEDs, and best-fit stellar population models for a variety of galaxies in the middle-redshift interval. The galaxies are ordered by decreasing UV-to-optical flux ratio. COSMOS-3623 is a young and unobscured star-forming galaxy with a strong Lyman break and a nearly absent Balmer break. GOODS-N-3449 is slightly more evolved with a stronger Balmer break. For AEGIS-28659 and AEGIS-28421, the UV gradually becomes dimmer and the Balmer break becomes stronger. Both galaxies have clearly detected emission lines. With AEGIS-17754, we continue the sequence of a gradually increasing Balmer break. GOODS-N-11745 is a very dusty star-forming galaxy. COSMOS-13577 and COSMOS-11982 both have SEDs indicative of a quiescent stellar population. COSMOS-13577 does have line emission, but the high ratio of [N II]/Hα indicates

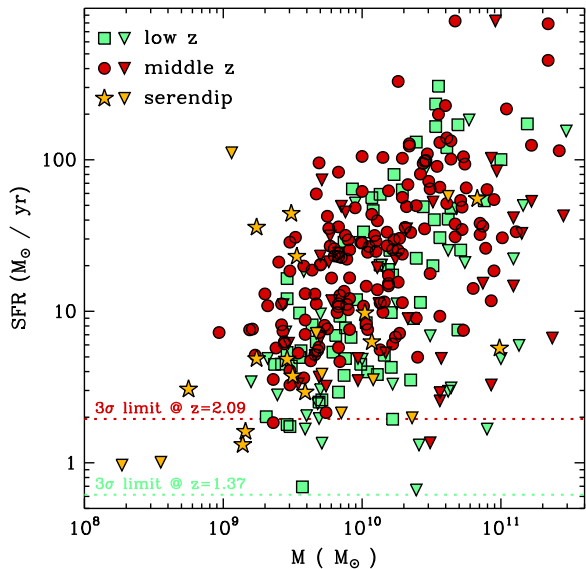**Figure 14.** SFR vs. stellar mass for galaxies in the low (green) and middle redshift interval (red) for a Chabrier IMF. The 3σ upper limits are indicated by the upside-down triangles. The yellow symbols indicate the galaxies that were serendipitously detected. The SFRs are derived from the combination of Hα and Hβ. The 3σ limits on the SFR, calculated using the optimal 3σ line sensitivities in H and K, are shown for $z \sim 1.37$ and $z \sim 2.09$ (i.e., the lower boundaries of the redshift intervals), respectively. In this calculation we assume no dust attenuation.

that it most likely originates from an AGN. For COSMOS-11982 no emission lines are detected, and thus we zoom in on the absorption lines.

4.6. Comparison to Full Galaxy Distribution

In the previous section we showed that our success rate is high. Nonetheless, we are missing 21% of the targeted galaxy population. In this section we assess whether our targeted and spectroscopically confirmed samples are representative of the full galaxy sample in the same redshift interval to the same magnitude limit, or whether we may be missing galaxies with specific properties. For this assessment we consider as the full galaxy population the parent sample within the targeted redshift regime down to the same H-band magnitude limit from which our spectroscopic sample was selected.

We first compare galaxies in the rest-frame $U - V$ color versus rest-frame $V - J$ color diagram (UVJ diagram). Galaxies out to $z \sim 2.5$ show a natural bimodality in this color–color space, and both the star-forming and quiescent galaxies span tight sequences (e.g., Wuyts et al. 2007; Williams et al. 2009; Whitaker et al. 2011). Thus, this diagram is used to isolate quiescent from star-forming galaxies and classify galaxies out to $z \sim 4$ (e.g., Muzzin et al. 2013a). The quiescent sequence is primarily an age sequence, with galaxies becoming redder in both colors with increasing age (e.g., Whitaker et al. 2012, 2013). The star-forming sequence primarily reflects the change in dust attenuation, with the dustiest galaxies having the reddest $U - V$ and $V - J$ colors (e.g., Brammer et al. 2011).

We derive rest-frame colors for all galaxies in the MOSDEF and parent samples, using the EAzY code (Brammer et al. 2008) and following the method described by Brammer et al. (2009). This method assumes a redshift and interpolates between different observed bands using templates that span the full range in galaxy properties. However, the derived colors are not pure template colors because the templates are only used to fit the photometric data points closest to and surrounding the specific rest-frame filter. When deriving rest-frame colors, we assume the MOSDEF or other spectroscopic redshifts when available. When no spectroscopic redshift is available, we assume the best-fit grism or photometric redshift.

In the left panels of Figure 16 we show UVJ diagrams with the parent distribution in gray scale and the targeted sample represented by the colored symbols. Each row represents a different redshift interval. Spectroscopically confirmed galaxies and AGNs are indicated by red circles and yellow stars, respectively. Because several MOSDEF redshifts lie outside the targeted redshift interval, we adjust the intervals for the confirmed galaxies to $1.25 \leqslant z \leqslant 1.9$, $1.9 < z \leqslant 2.61$, and $2.94 \leqslant z \leqslant 3.80$. Targeted galaxies and AGNs for which no spectral features are detected, or for which the spectroscopic redshifts are not robust, are represented by green boxes and blue triangles, respectively. For these latter galaxies, rest-frame colors are derived by assuming the prior redshift or nonrobust MOSDEF redshift, respectively. The histograms show the distribution of $U - V$ and $V - J$ colors for the parent sample in black and the spectroscopically confirmed sample (both galaxies and AGNs) in red.

The location of galaxies in the UVJ diagram is dependent on mass, with more massive galaxies populating the red sequence and the dusty part of the star-forming sequence (e.g., Williams et al. 2010). In order to further compare our sample to the parent population, we show H_{F160W} magnitude versus stellar mass for the parent and targeted galaxies in the right panels of Figure 16, using the same symbols as in the left panels. For galaxies and AGNs for which no spectroscopic features are detected, we derive stellar masses assuming prior redshift information. The distributions in stellar mass and H_{F160W} magnitude for the parent and spectroscopically confirmed samples are presented by the black open and red shaded histograms, respectively.

For all redshift ranges, our targeted sample is distributed over the full UVJ diagram; we target galaxies along the entire star-forming and quiescent sequences. The histograms show that the distribution of rest-frame $U - V$ and $V - J$ colors of the parent and confirmed samples are similar for the middle- and high-redshift intervals. In the low-redshift interval we miss more galaxies with the reddest $U - V$ colors, which we discuss in more detail in the next section. As in the parent sample, the majority of the confirmed galaxies are blue in both colors, and thus our sample is dominated by blue star-forming galaxies. Red star-forming and quiescent galaxies form a minority in our sample.

The small fraction of red star-forming and quiescent galaxies may not be surprising because these galaxies primarily populate the high-mass end of the galaxy distribution and thus will be sparse for a galaxy sample with a mass limit of $\sim 10^9 \, M_{\odot}$. However, in our selection scheme, we specifically aim to obtain a roughly flat distribution in H_{F160W} magnitude and stellar mass, and thus we prioritize galaxies by H_{F160W} magnitude. The right panels in Figure 16 indeed show that our sample is biased toward brighter and slightly more massive galaxies compared to the parent sample. The fact that our H_{F160W} prioritization did not result in a bias toward redder rest-frame $U - V$ and $V - J$ colors is due to the lower spectroscopic success rate of red galaxies.
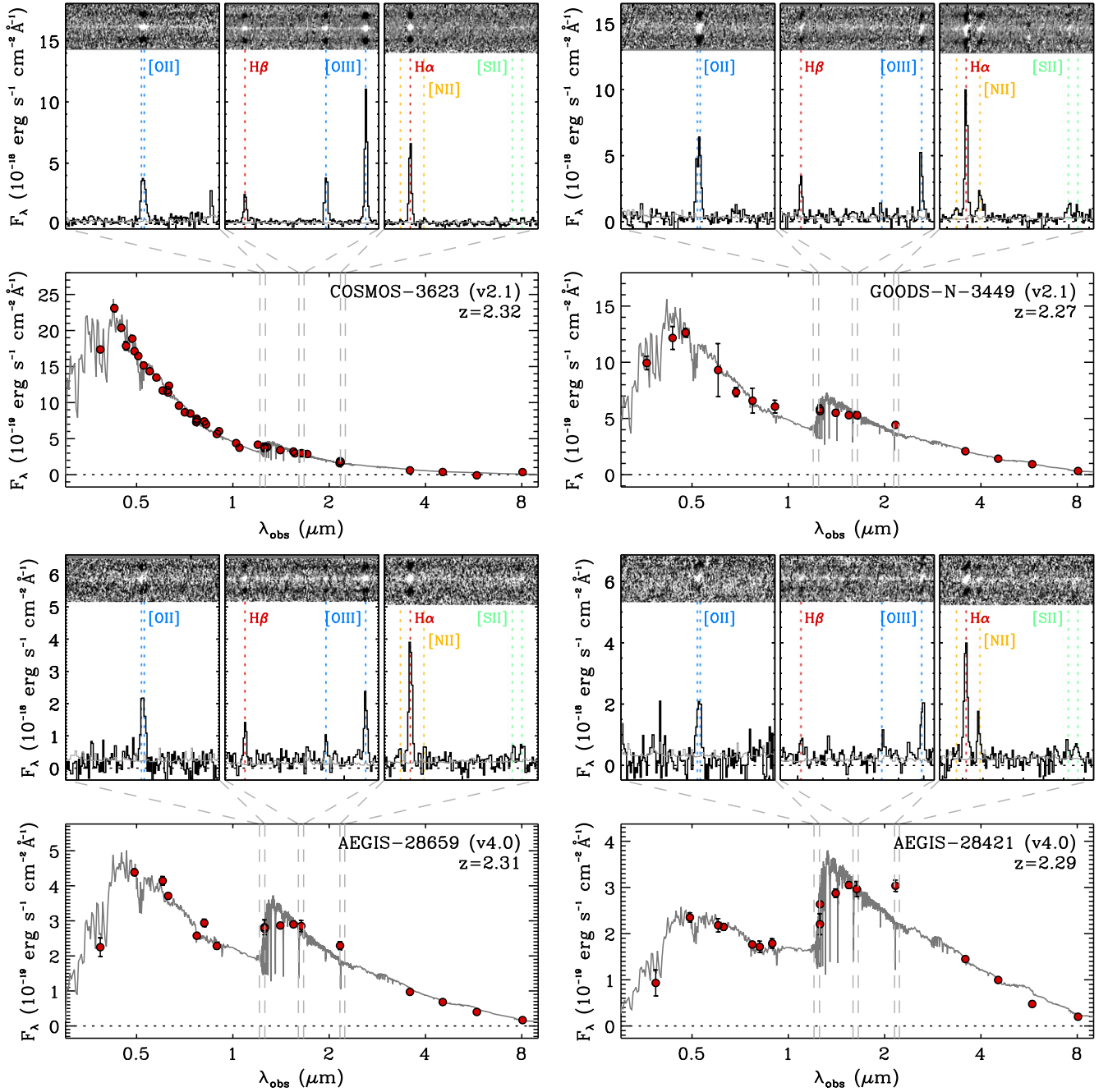
Figure 15. Example MOSFIRE spectra and corresponding multiwavelength SEDs for eight galaxies in the middle MOSDEF redshift regime. The galaxies have different SED shapes and are ordered by decreasing UV-to-optical flux. The lower panels show the rest-frame UV to near-IR photometry from the 3D-*HST* photometric catalogs (Skelton et al. 2014) and the best-fit stellar population model. The dashed vertical lines indicate the wavelength intervals for which we show the MOSFIRE spectra in the top panels. With the exception of COSMOS-11982, the top panels show both the 1D and 2D MOSFIRE spectra in the wavelength regions around the [O II] doublet, Hβ and [O III], and Hα, [N II], and [S II], from left to right, respectively. Thus, we only show selected regions of the full MOSFIRE spectra. For COSMOS-11982 we zoom in around the absorption lines Ca II H and K in the J band and Mgb in the H band. All 1D spectra except for COSMOS-11982 J-band spectra are binned by three pixels in the wavelength direction, while excluding very noisy wavelengths (i.e., corresponding to the locations of sky lines), and are shown in black. For the COSMOS-11982 J band, we binned the spectra by seven pixels. The binned noise spectra are shown in gray. For clarity, the 2D spectra have been stretched in the vertical direction by a factor of two.

4.7. Success Rate for Different Galaxy Types

In order to assess the spectroscopic success rate for different types of galaxies, we split the *UVJ* diagram into three regions—quiescent galaxies, blue star-forming galaxies, and red star-forming galaxies—and give the success rate for each galaxy class in Figure 16. For all redshift intervals, the success rate is highest (∼90%) for blue star-forming galaxies. Red star-forming galaxies have a lower success rate, which varies from 27% in the

highest redshift interval to 75% in the middle redshift interval. Quiescent galaxies have the lowest success rate, varying from 9% in the low-redshift interval to 50% in the middle-redshift interval.

We also show the fraction of confirmed to targeted galaxies as a function of stellar mass, H-band magnitude, rest-frame $U - V$ color, and rest-frame $V - J$ color in Figure 17. This figure illustrates that success rate primarily correlates with rest-frame $U - V$ color. The success rate also slightly decreases
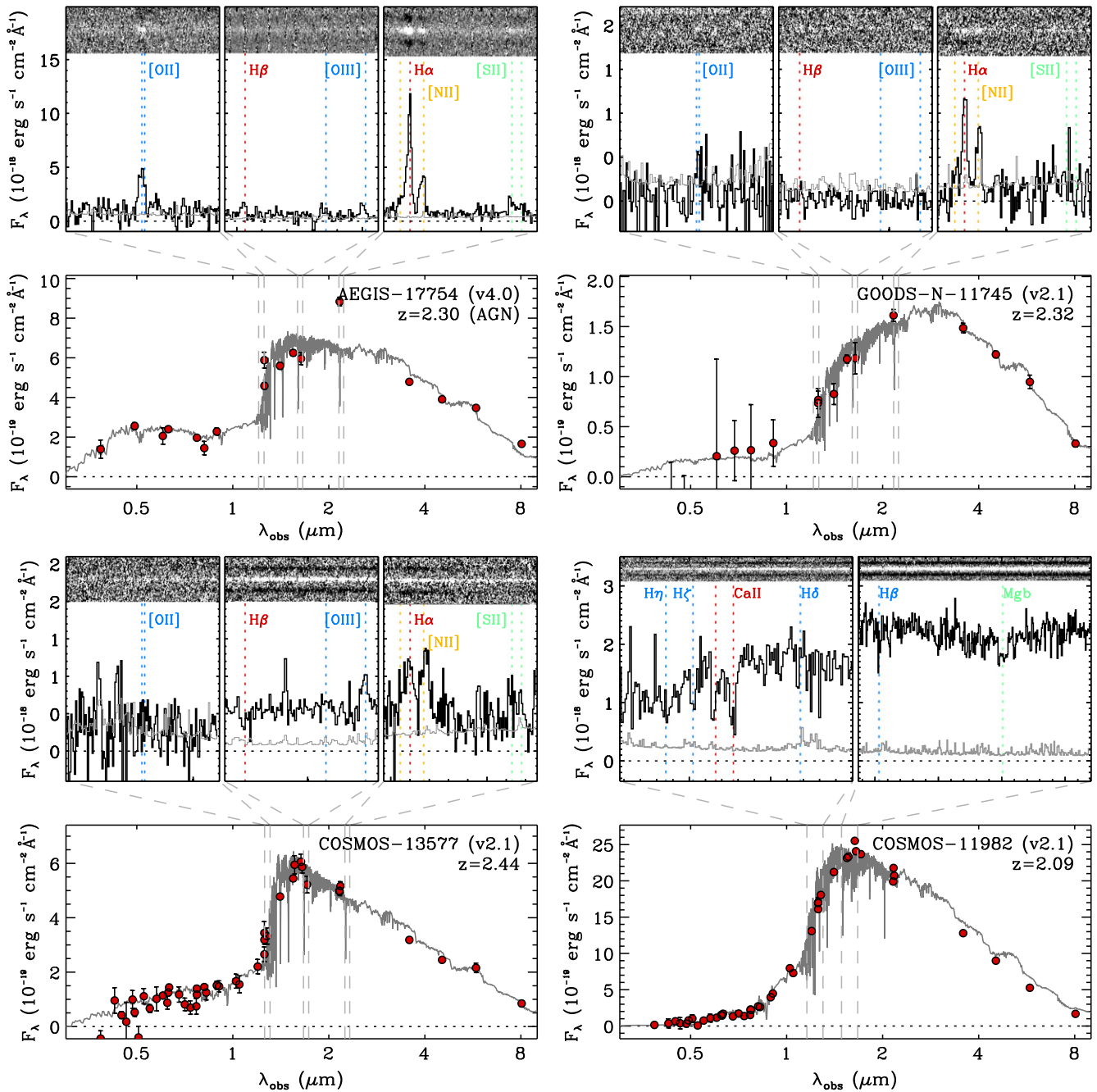
Figure 15. (Continued.)

with increasing stellar mass, which reflects the larger fraction of red galaxies at the high-mass end of the galaxy distribution.

We examine the possible causes affecting the success rate for the different galaxy types. We first assess whether our prioritization scheme may affect the difference in the success rate between the different classes. In our selection we prioritize galaxies with prior spectroscopic redshifts. For these galaxies we are more confident that the spectral lines will fall in observable parts of the spectrum than for galaxies with just photometric redshifts. Furthermore, the fact that these galaxies had prior spectroscopic redshifts may suggest that they are bright or have strong spectral features. Thus, if the prioritization by prior spectroscopic redshift favors a particular galaxy

type, it could lead to a higher success rate for that class. In Figure 18 we show the *UVJ* diagram for all targeted galaxies, with the red circles indicating the confirmed galaxies for which we had a correct prior spectroscopic redshift. Interestingly, the fraction of galaxies with prior spectroscopic redshifts compared to all confirmed galaxies does not vary with galaxy type (~36%). Hence, for all types we increase the number of galaxies with spectroscopic redshifts by a factor of about three. Thus, our prioritization by prior spectroscopic redshift is not contributing to the higher success rate for blue star-forming galaxies.

Another possible cause for the lower success rate of red galaxies may be the decreasing strength of emission lines in
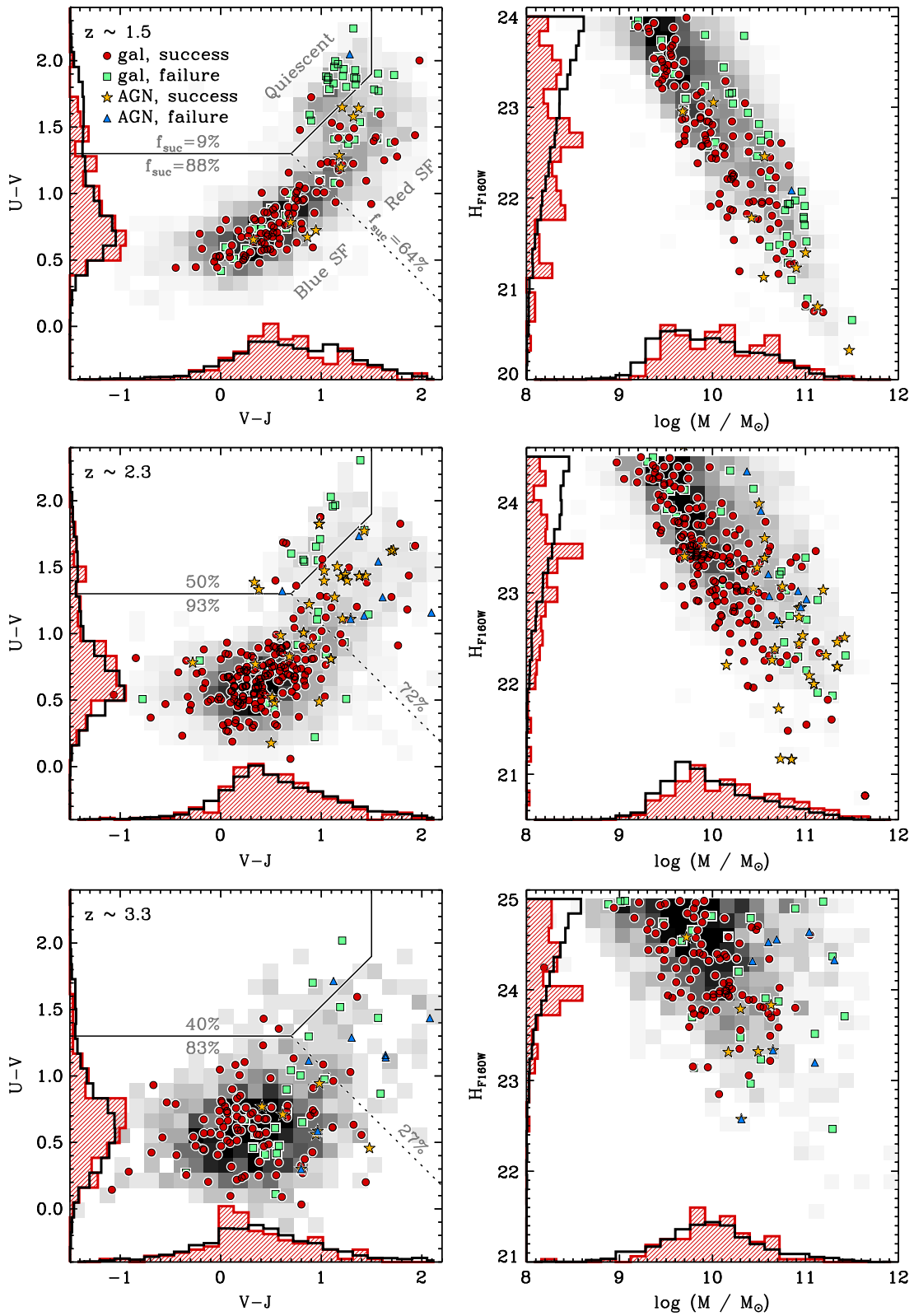
Figure 16. Left: rest-frame $U - V$ vs. $V - J$ color (UVJ diagram) for the three different redshift intervals. Quiescent galaxies populate the sequence enclosed by the box in the top left of this diagram. Star-forming galaxies populate the bottom sequence. In gray scale we show the parent galaxy samples from which the targets are selected, with H-band magnitude limits of 24.0, 24.5, and 25.0, for the low-, middle-, and high-redshift intervals, respectively. The colored symbols represent our targeted objects, with red circles and yellow stars indicating galaxies and AGNs with robust spectroscopic redshifts. The green squares and blue triangles indicate targeted galaxies and AGNs for which no robust redshifts have been obtained. AGNs are identified by either their X-ray luminosity or IRAC colors (Coil et al. 2014). The success rate for quiescent galaxies, blue star-forming galaxies (below/to the left of the dotted line), and red star-forming galaxies (above/to the right of the dotted line) are given in gray. The open black and shaded red histograms represent the distribution of the parent and confirmed samples (galaxies and AGNs), respectively, for the property on the corresponding axis. The histograms are normalized to the same area. Right: H_{F160W} magnitude vs. stellar mass for the parent sample (gray scale) and the MOSDEF targeted galaxies and AGNs. Symbols and histograms are similar to those in the left panels.
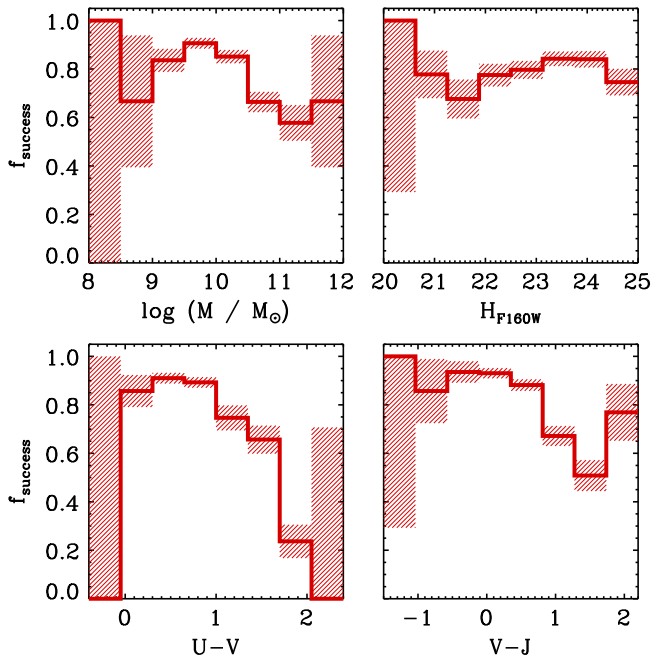
Figure 17. Success rate as a function of stellar mass (top left), H-band magnitude (top right), rest-frame $U - V$ color (bottom left), and rest-frame $V - J$ color (bottom right). The success rate is defined as the ratio of targeted galaxies with robust MOSDEF spectroscopic redshift to the total sample of targeted galaxies. The shaded regions indicate the uncertainties in the ratios. Serendipitous detections are excluded. The success rate primarily correlates with rest-frame $U - V$ color.

redder galaxies. The star-forming sequence is thought to be a sequence of increasing dust attenuation, and redder galaxies may therefore have fainter emission lines. To assess this theory, we show the *UVJ* diagram in Figure 18(b) color coded by the ratio of Hα/Hβ. We find that the Hα/Hβ ratio is indeed higher for red star-forming galaxies, indicative of more dust extinction (see Reddy et al. 2015). However, to assess whether the larger dust extinction results in lower line fluxes, we color code the *UVJ* diagram by the flux of the strongest emission line in Figure 18(c). Interestingly, the blue and red star-forming galaxies have the same median flux of $10^{-16.2}$ erg s^{-1} cm^{-2}. However, this finding does not rule out that we may miss fainter emission lines for the redder star-forming population. We do note that the average number of detected emission lines for blue star-forming galaxies is higher than for red star-forming galaxies, with 2.8 and 2.3, respectively.

Yet another possibility for the lower success rate of red star-forming galaxies may be the more uncertain photometric redshifts compared to those of blue star-forming galaxies. To test this scenario, in Figure 18(d) we color code all galaxies with a MOSFIRE redshift, but without a prior spectroscopic redshift by $\Delta z/(1 + z)$, the difference in redshift between their prior and MOSDEF redshift. With a median $\Delta z/(1 + z)$ of 0.026, red star-forming galaxies have the most uncertain prior redshifts, but the difference among the different galaxy types is small. In order to identify the primary reason for the lower success rate of red star-forming galaxies, we would need emission-line measurements and spectroscopic redshifts for star-forming galaxies that have not been confirmed.

For quiescent galaxies, we find that the faint emission-line fluxes are contributing to the low success rate. Given that the

galaxies in the quiescent box have much lower SFRs, we indeed expect to find little or no line emission. Nonetheless, for $z \sim 2.3$, about half of the galaxies in the quiescent box have detected emission lines. This result is consistent with the results from Kriek et al. (2008a), who find that about 40% of the quiescent galaxies at $z \sim 2.3$ have line emission. To test whether the line emission from our quiescent galaxies originates from AGNs, we color code all galaxies in the *UVJ* diagram by [N II]/Hα ratio (Figure 18(e); see also Coil et al. 2014). For half of the galaxies in the quiescent box with emission lines for which we can measure [N II]/Hα, we indeed find a high ratio (>0.6), indicative of an AGN.

For quiescent galaxies we can also measure spectroscopic redshifts from absorption lines. We only measured absorption line redshifts for two $z \sim 2.3$ quiescent galaxies. To assess why this fraction is so low, we color code the *UVJ* diagram by the continuum S/N per pixel in the band that targets the 4000 Å break because this wavelength region covers several strong absorption lines. Figure 18(f) shows that most quiescent galaxies have a very low S/N in this wavelength region, and 18% of the quiescent galaxies (three masks) lack data in this wavelength region altogether. The galaxies with low S/N and missing wavelength coverage are primarily in the low-redshift masks. Three out of the six low-redshift masks were observed during bad weather conditions, and the nominal integration time for this redshift interval is shorter than for the higher redshift masks. The integration times were shortened because, in general, galaxies are brighter at lower redshift. However, as suggested by their location in the *UVJ* diagram, quiescent galaxies at $z \sim 1.5$ are likely older with lower M/L and thus may be more challenging to confirm (Whitaker et al. 2012). In addition, the fraction of quiescent galaxies with emission lines is lower at $z \sim 1.5$. These factors together may explain the very low success rate of the $z \sim 1.5$ quiescent galaxies.

In summary, the low success rate of quiescent galaxies is primarily due to the low fraction of quiescent galaxies with detected line emission and the low S/N or missing continuum emission around the 4000 Å break for most quiescent galaxies. Red star-forming galaxies have brighter emission lines and a higher fraction of galaxies with detected line emission, and thus they have a higher success rate than quiescent galaxies. However, the success rate for red star-forming galaxies is lower than for blue star-forming galaxies. The difference in success rates between these two galaxy types is not well understood.

5. SCIENCE OBJECTIVES OF MOSDEF

The MOSDEF data set allows a wide range of new and unique studies, which all contribute to constructing a complete picture of galaxy formation. Most science cases rely on a combination of MOSDEF rest-frame optical spectroscopy and other multiwavelength data sets available in the targeted fields. In this section we briefly summarize our primary science objectives.

5.1. Star Formation and the Mass Growth of Galaxies

A fundamental aspect of the study of galaxy evolution is understanding how galaxies build their stellar mass over cosmic time. By tracing both the evolution in stellar mass and SFR of a complete galaxy sample, we can constrain the rate and
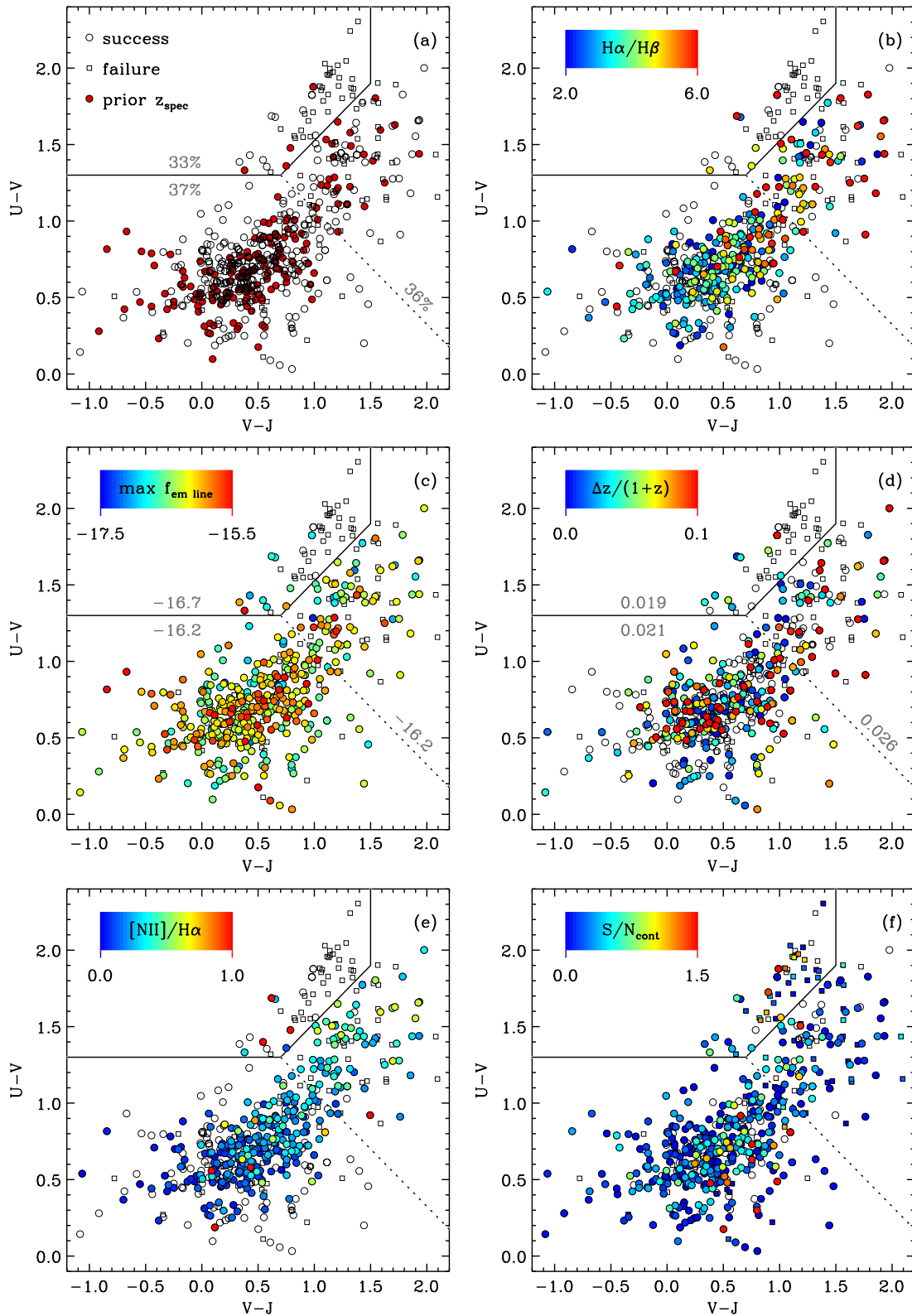
Figure 18. Assessment of spectroscopic success rate for different spectral types using the *UVJ* diagram. Galaxies with and without robust MOSDEF spectroscopic redshifts are indicated by circles and squares, respectively. (a) Galaxies with correct prior spectroscopic redshifts are indicated in red. The fraction of prior to MOSDEF spectroscopic redshifts (given in the panel) does not vary with spectral type. (b–c) Galaxies are color coded by the ratio of $H\alpha/H\beta$ and the flux of the brightest emission line ($\log(f/(\mathrm{erg\ s^{-1}\ cm^{-2}}))$), when available. Red star-forming galaxies are more dusty, as indicated by their higher $H\alpha/H\beta$ ratio, but the median line emission (given in panel c) is the same for blue and red star-forming galaxies. (d) Galaxies with MOSDEF redshifts but without prior spectroscopic redshifts are color coded by $\Delta z/(1 + z)$, with the median value given for each class. Red star-forming galaxies have the least certain prior redshifts, but the difference is small. (e) Galaxies are color coded by the ratio of [N II]/$H\alpha$, when available. This panel shows that for half of the quiescent galaxies for which we can measure this ratio, the line emission likely originates from an AGN. (f) All targeted galaxies are color coded by the median continuum S/N per pixel in the band that targets the 4000 Å break. The S/N for most quiescent galaxies is too low to measure absorption lines, or a spectrum is missing altogether.

by which mechanism (star formation versus mergers) galaxies grow (e.g., van Dokkum et al. 2010; Reddy et al. 2012b). However, deriving both properties is challenging. In particular, SFRs of $z > 1$ galaxies are highly uncertain because of the inaccessibility of reliable indicators (Hα and Hβ; bolometric flux).

With MOSDEF we detect—for the first time—both the Hα and Hβ emission lines for a large rest-frame optical magnitude-limited sample of distant galaxies. These features together form the ideal SFR indicator, which is relatively unbiased to dust extinction (unlike the UV continuum emission). Using the multiwavelength data in the CANDELS fields, we will compare our SFRs with SFRs derived using other indicators (e.g., UV, *MIPS* 24 μm, *Herschel*) to better calibrate SFR indicators and to obtain a full census of star formation at high redshift. MOSDEF also improves the accuracy of stellar mass measurements by providing spectroscopic redshifts and estimates of the contribution of line emission to the photometric fluxes.

5.2. Dust Attenuation

A key aspect of quantifying SFRs is understanding how the intrinsic galaxy spectrum is modulated by interstellar dust. Unfortunately, even the deepest *Spitzer* and *Herschel* mid- to far-IR observations are insufficient to directly detect dust emission from individual $L*$ galaxies at $z \gtrsim 2$ (e.g., Reddy et al. 2010, 2012a). Consequently, we are reliant on stellar population modeling and the UV slope β, whose use for estimating dust attenuation in particular types of galaxies has been called into question by many studies (e.g., Kong et al. 2004; Siana et al. 2009; Reddy et al. 2010; Kriek & Conroy 2013).

MOSDEF will enable the measurement of one of the most direct and locally well-studied dust indicators, the Balmer decrement (Hα/Hβ), for a statistical sample of $1.4 \lesssim z \lesssim 2.6$ galaxies. Previous such measurements primarily relied on stacked spectra (e.g., Domínguez et al. 2013; Price et al. 2014) or very small samples of individual galaxies. Using the multiwavelength data in the MOSDEF survey fields, we will cross-check dust corrections inferred from the Balmer decrement, UV slope, and (stacked) mid- and far-IR emission and build a complete census of dust properties of $z \sim 2$ galaxies (e.g., dust-to-star geometry, temperature). In a first paper (Reddy et al. 2015), we present Balmer decrements for $z \sim 2$ star-forming galaxies and derive their dust attenuation curves.

5.3. Gas-phase Metallicities

The metal content of galaxies reflects the past integral of star formation, modified by the effects of gas inflow (i.e., accretion) and outflow (i.e., feedback). Whereas the mass–metallicity relationship has been measured for large samples of star-forming galaxies at $z < 1$ (Tremonti et al. 2004; Moustakas et al. 2011), observations of this trend at higher redshifts have until recently been based on either small or biased samples of individual objects (Mannucci et al. 2009) or on composite spectra that mask the variation among individual objects (Erb et al. 2006).

With MOSDEF we derive gas-phase metallicities for many individual galaxies from a suite of bright rest-frame optical emission lines. In a first paper (Sanders et al. 2015), we correlate gas-phase metallicity with stellar mass and the SFR of 86 star-forming galaxies and show that high-redshift galaxies do not fall on the local "fundamental metallicity relation" (Mannucci et al. 2009) among stellar mass, metallicity, and SFR (see also Steidel et al. 2014).

5.4. ISM Physical Conditions

Measurements of multiple rest-frame optical emission lines are crucial for understanding the physical conditions in the ISM of high-redshift galaxies. At low redshift, star-forming galaxies follow a fairly tight sequence in the space of [N II]/Hα versus [O III]/Hβ, also known as the BPT diagram (Baldwin et al. 1981). However, small samples of $z > 1$ galaxies with measurements of Hβ, [O III], Hα, and [N II] appear to be systematically offset from the excitation sequence of low-redshift galaxies (e.g., Shapley et al. 2005). The origin of these differences may reflect fundamental differences in distant H II regions (e.g., Brinchmann et al. 2008; Liu et al. 2008) and may have severe implications for metallicity measurements of galaxies.

MOSDEF significantly increases the number of distant galaxies with Hα, Hβ, [O III], and [N II] emission-line measurements, such that we can accurately measure their location in the BPT diagram. Measurements of [O II] and [S II] enable studies of additional ISM excitation diagrams. In a first paper (Shapley et al. 2015), we confirm the offset of the excitation sequence and assess how the offset varies with stellar mass, specific SFR, and SFR surface density of $z \sim 2.3$ galaxies.

5.5. Stellar Feedback

The process described as "feedback" is considered a crucial component in models of galaxy formation. Feedback commonly refers to large-scale outflows of mass, metals, energy, and momentum from galaxies, regulating the amount of gas available to form stars, as well as the thermal properties and chemical enrichment of the intergalactic medium. However, directly observing the inflow of gas into galaxies—especially during the epoch when they are assembling—remains challenging.

Using nebular emission lines in the MOSDEF spectra in combination with existing and new UV spectroscopy,[25] we will measure the speed of outflowing (blueshifted) or inflowing (redshifted) gas and correlate this speed with galaxy properties such as (specific) SFR, SFR surface density, inclination, and size. In addition, the resolution of MOSFIRE spectra will allow for detailed profile fitting of the strongest rest-frame optical emission lines, which will highlight deviations from symmetric Gaussian profiles or underlying broad components, which may be indicative of extended, outflowing ionized gas (Genzel et al. 2011; Newman et al. 2012b).

5.6. Nuclear Accretion and Galaxy Coevolution

Determining the causes and evolution of AGN triggering and fueling is essential to understanding the formation and evolution of both black holes and galaxies. Accretion onto supermassive black holes appears to peak at a redshift of $z \sim$ 1–3 (e.g., Hasinger et al. 2005), though the exact location of this peak and its dependence on black hole mass and AGN

---

[25] We are conducting a complementary observing campaign to obtain rest-frame UV spectroscopy for MOSDEF galaxies with DEIMOS.

luminosity are still unknown. The physical relationship between AGN and their host galaxies at this key epoch is also unclear. It has been difficult to make progress on these questions because of the small number of AGNs at these epochs for which rest-frame optical emission lines have been measured.

The MOSDEF spectra allow us to optically identify AGN using the BPT diagram. We will complement the BPT diagram with X-ray and mid-IR color selection criteria and quantify the fraction of galaxies that host an AGN over cosmic time. We will also use the [O III] luminosity of AGNs to probe black hole accretion at $z \sim 2$ and quantify the connection between black hole and galaxy growth by relating the AGN fraction and accretion rates to host galaxy properties. In a first paper (Coil et al. 2015), we test various optical AGN classification diagnostics at $z \sim 2$, including the BPT, MEx (Juneau et al. 2011), and CEx diagrams (Yan et al. 2011).

5.7. Dynamical Masses and Structural Evolution

During the peak of star formation activity, massive galaxies ($>10^{11} M_\odot$) show a wide diversity in galaxy properties, with the population about equally divided between star-forming and quiescent galaxies (e.g., Kriek et al. 2008a; Muzzin et al. 2013b). These galaxies are not simply the younger versions of elliptical and star-forming galaxies today, but were smaller and denser at similar mass (e.g., Williams et al. 2010). Both populations appear to grow inside out, but the physical mechanism (e.g., minor mergers, progenitor bias, cold streams, and in situ star formation) responsible for the growth is still subject to debate (e.g., Dutton et al. 2011; Newman et al. 2012a; Carollo et al. 2013; van Dokkum et al. 2013; van de Sande et al. 2013).

Identifying the dominant growth mechanism for both quiescent and star-forming galaxies requires accurate mass, kinematic, and size measurements for a large and complete sample of distant galaxies. With MOSDEF we measure velocity dispersions from rest-frame optical nebular emission and stellar absorption lines. Combined with high-resolution rest-frame optical imaging from CANDELS, we will measure dynamical masses and study how both quiescent and star-forming galaxies grow in size, velocity dispersion, and mass over cosmic time.

6. SUMMARY

In this paper, we present the MOSDEF survey, a 47 night program with MOSFIRE on the Keck I Telescope, to obtain intermediate-resolution ($R = 3000$–3650) rest-frame optical spectra for ~ 1500 galaxies at $1.37 \leqslant z \leqslant 3.80$. The survey is being executed in three well-studied extragalactic legacy survey fields (AEGIS, COSMOS, and GOODS-N) and will cover ~ 600 square arcminutes. The galaxy sample is split into three redshift intervals ($1.37 \leqslant z \leqslant 1.70$, $2.09 \leqslant z \leqslant 2.61$, and $2.95 \leqslant z \leqslant 3.80$), for which bright rest-frame optical emission lines ([O II], Hβ, [O III], Hα, [N II], and [S II]) fall in atmospheric windows. Emphasis is given to the middle redshift interval, which will contain half of our sample. The remaining galaxies will be evenly split among the lower and higher redshift intervals. The galaxies are selected using the multiwavelength photometric and spectroscopic catalogs from the 3D-*HST* survey down to a fixed H-band magnitude. The magnitude limits are $H = 24.0$, $H = 24.5$, and $H = 25.0$, for the low-,

middle-, and high-redshift interval, respectively. Priority is given to brighter galaxies, galaxies with more reliable redshifts, and galaxies hosting an AGN.

MOSDEF is scheduled to be executed over four spring semesters, and we have currently completed our second observing semester. To date, we have obtained rest-frame optical spectra for 591 targeted galaxies. We have developed a fully automated 2D data reduction pipeline, optimized for low S/N sources. The combination of our observational strategy and custom reduction software leads to an improvement in S/N of up to 25% compared to standard procedures. All spectra are optimally extracted, and all emission lines are measured using a Gaussian fitting procedure. For galaxies without line emission but with bright continuum emission, we measure rest-frame optical absorption lines. We derive both continuum and line sensitivities and show that the theoretical expectations for the continuum emission are optimistic by a factor of about two. For average weather conditions, MOSFIRE yields an S/N ~ 3 per pixel within 2 hr in the H band for galaxies with a total magnitude of $H = 22$. A 5σ detection for an emission line within 2 hr requires a total emission-line flux of $\gtrsim 1.5 \times 10^{-17}$ erg s^{-1} cm^{-2}.

With integration times of 1–2 hr per filter, we derive robust redshifts based on emission lines for 462 out of 591 targeted galaxies. Including three additional spectra for which we robustly identify multiple absorption lines, we achieve a success rate of 79%. Of the 465 confirmed galaxies, 31 galaxies have been observed twice. Thus, the number of unique targets with robust spectroscopic redshifts is 434. In addition, we measure robust spectroscopic redshifts for 55 galaxies that were serendipitously detected. For 64% of the spectroscopically confirmed primary targets, there was no robust spectroscopic redshift prior to MOSDEF.

We derive stellar population properties for all MOSDEF galaxies by fitting the photometric SEDs with stellar population models, while assuming the MOSDEF redshifts. We also derive SFRs from the combination of the Hα and Hβ emission lines. The stellar masses of our spectroscopically confirmed sample are in the range $\sim 10^9$–$10^{11.5} M_\odot$ and the SFRs are in the range $\sim 10^0$–$10^3 M_\odot$ yr^{-1}. Our spectroscopic sample exhibits a wide variety of galaxy properties and ranges from unobscured star-forming galaxies, to dusty star-forming galaxies, to those with quiescent stellar populations.

The spectroscopic success rate correlates with galaxy type and is highest for blue star-forming galaxies ($\sim 90\%$). For red star-forming galaxies, the spectroscopic success rate is lower and varies from 27% (high-redshift interval) to 75% (middle-redshift interval). The spectroscopic success rate is lowest for quiescent galaxies and ranges from 9% (low-redshift interval) to 50% (middle-redshift interval). Quiescent galaxies are more challenging to confirm because emission lines are generally faint or absent, and absorption lines can only be detected for the brightest galaxies ($H \lesssim 22$). The success rate is particularly low for quiescent galaxies in the $z \sim 1.5$ sample, primarily due to poorer weather conditions, the lack of spectra sampling the Balmer/4000 Å break regions, and the smaller fraction of quiescent galaxies with emission lines. We have not identified a clear cause for why the spectroscopic success rate for red star-forming galaxies is lower than for blue star-forming galaxies.

We compare our MOSDEF sample to the parent galaxy sample at the same redshift from which our targets were drawn.

Despite the lower success rate for red galaxies, our prioritization by H-band magnitude ensured a representative distribution in rest-frame $U - V$ and $V - J$ colors for the middle- and high-redshift intervals. In the low-redshift interval we miss the galaxies with the reddest $U - V$ rest-frame color because of the lower success rate of red galaxies compared to the other redshift intervals.

With its large sample size, its broad diversity of galaxies, its large dynamic range in mass, SFR, and redshift, and the availability of a wealth of ancillary data in the targeted fields, the MOSDEF survey will open up a broad range of unique science projects. Our science objectives range from the star formation and dust properties of distant galaxies, to the chemical enrichment history of galaxies, to the physical properties of the ISM in the early universe, to the accretion histories of black holes, and the structural evolution and mass growth of galaxies over cosmic time. Early science papers, based on data obtained during the first semester(s), focus on the relation between gas-phase metallicity, stellar mass, and SFR (Sanders et al. 2015), the excitation properties of H II regions (Shapley et al. 2015), dust attenuation (Reddy et al. 2015), and the identification of AGNs (Coil et al. 2015) in $z \sim 2.3$ galaxies. MOSDEF will be complemented by forefront theoretical investigations and simulations that will help refine current models of galaxy evolution, ISM, and black hole coevolution. All MOSDEF data products, including the 2D and 1D reduced spectra, spectroscopic redshifts, and value-added catalogs, will be made publicly available during and upon completion of the project.[26]

APPENDIX
DITHER PATTERN

In this section we show why different dither sequences result in different S/N measurements of the reduced spectra. For an ABBA dither sequence, we use the frame before or after the exposure as sky:

$$f_{i,s} = f_i - f_{i\pm1}. \quad (8)$$

We define the noise in a single raw image i as σ_i. The noise level of the sky-subtracted image then becomes

$$\sigma_{i,s} = \sqrt{\sigma_i^2 + \sigma_{i\pm1}^2}. \quad (9)$$

Given that the noise level of two subsequent images is approximately the same, we find

$$\sigma_{i,s} = \sqrt{2}\,\sigma_i. \quad (10)$$

For an ABA′B′ dither pattern (see Figure 19), we can use the average of the two surrounding science frames as the sky frame:

$$f_{i,s} = f_i - \frac{f_{i-1} + f_{i+1}}{2}. \quad (11)$$

The noise in the sky-subtracted frames now becomes

$$\sigma_{i,s} = \sqrt{\sigma_i^2 + \left(\frac{\sigma_{i-1}}{2}\right)^2 + \left(\frac{\sigma_{i+1}}{2}\right)^2} = \sqrt{\frac{3}{2}}\,\sigma_i. \quad (12)$$

Thus, the noise level in the sky-subtracted frames for the ABA′B′ pattern is $\frac{\sqrt{3/2}}{\sqrt{2}} = \sqrt{3/4}$ times lower than the noise level for a classic ABBA dither pattern.

For an ABAB dither pattern (see Figure 19), we can also use the average of two surrounding sky frames to subtract from each science frame. For an individual science frame, the noise level decreases as well by a factor of $\sqrt{3/4}$ for this dither pattern. However, this effect cancels out when we combine all individual science frames to make the final spectrum, as shown below.

Consider the dither sequence $..., A_{i-1}, B_{i-1}, A_i, B_i, A_{i+1}, B_{i+1}, ...$ If we now add up three sky-subtracted science frames, all at A positions, we get

$$A_{i-1,s} + A_{i,s} + A_{i+1,s} = A_{i-1} - \left(\frac{B_{i-2} + B_{i-1}}{2}\right)$$
$$+ A_i - \left(\frac{B_{i-1} + B_i}{2}\right)$$
$$+ A_{i+1} - \left(\frac{B_i + B_{i+1}}{2}\right) \quad (13)$$

$$= -\frac{B_{i-2}}{2} + A_{i-1} - B_{i-1} + A_i - B_i$$
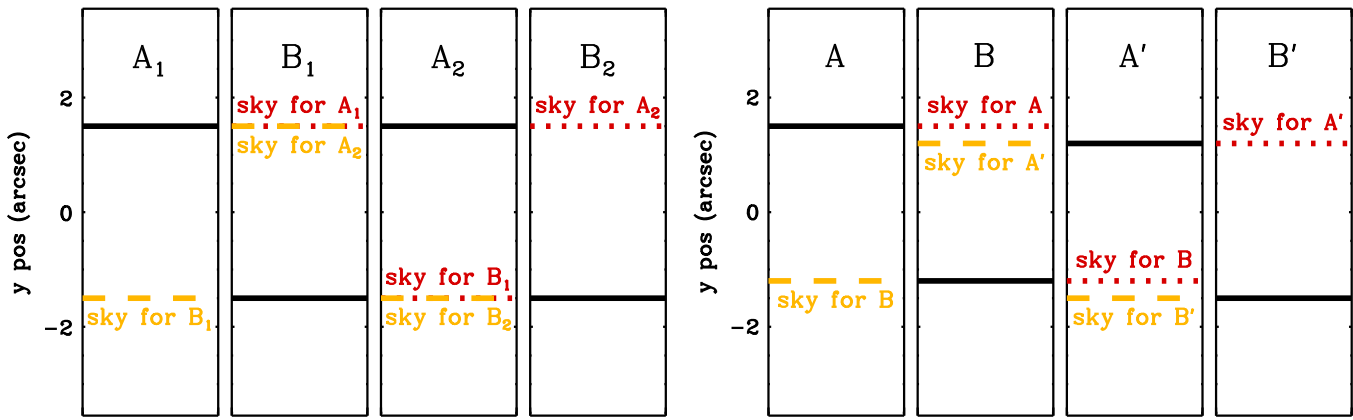$$+ A_{i+1} - \frac{B_{i+1}}{2}. \quad (14)$$

Figure 19. Illustration of the ABAB (left) and ABA′B′ (right) dither patterns. The horizontal black lines indicate the four dither positions for both dither sequences. The red dotted lines show the position of the sky used in the surrounding frames for the A dither positions. The yellow dashed lines show the position of the sky used in the surrounding frames for the B dither positions. This figure illustrates that for an ABA′B′ dither pattern, different regions of the detector of frame B are used as sky for A and A′. For the ABAB dither pattern, the same regions are used as sky for the two surrounding science frames.

For an infinitely long sequence this becomes

$$A_s = \sum_i A_i - B_i. \tag{15}$$

Thus, the ABAB dither sequence gives an approximately similar S/N level in the reduced spectrum as in the ABBA dither sequence.

However, for an ABA′B′ dither sequence, when adding up the sky-subtracted frames $A_{i,s}$ and $A'_{i,s}$, we get the following expression:

$$A_{i,s}(y) + A'_{i,s}(y + dy) = A_i(y)$$
$$- \left(\frac{B'_{i-1}(y) + B_i(y)}{2} \right) + A'_i(y + dy)$$
$$- \left(\frac{B_i(y + dy) + B'_i(y + dy)}{2} \right) \tag{16}$$

with dy the shift between A_i and A'_i. In this equation, $B_i(y)$ and $B_i(y + dy)$ cannot simply be added, and thus this expression cannot be simplified further. Hence, by shifting A_i slightly compared to A_{i+1}, we use different rows of the detector of B_i as the sky frame for A_i and A'_i, as also illustrated in Figure 19. To obtain the maximum S/N improvement of a factor of $\sqrt{3/4}$ in the 2D science frames, the offset between A and A′ needs to be at least one pixel. Otherwise, B'_{i-1} and B_i in the above equation are not independent. For a 1D extracted spectrum, different rows will be added together, and thus the S/N is highest if the extraction aperture is smaller than dy. For our dither sequence and average seeing conditions, this is not the case. However, because we use an optimal extraction method, for which the most weight is given to the central rows, the dither pattern will reduce the noise, despite the small value for dy.

REFERENCES

Atek, H., Malkan, M., McCarthy, P., et al. 2010, ApJ, 723, 104
Baldwin, J. A., Phillips, M. M., & Terlevich, R. 1981, PASP, 93, 5
Barger, A. J., Cowie, L. L., & Wang, W.-H. 2008, ApJ, 689, 687
Belli, S., Newman, A. B., Ellis, R. S., & Konidaris, N. P. 2014, ApJL, 788, L29
Bertin, E., & Arnouts, S. 1996, A&AS, 117, 393
Brammer, G. B., van Dokkum, P. G., & Coppi, P. 2008, ApJ, 686, 1503
Brammer, G. B., van Dokkum, P. G., Franx, M., et al. 2012, ApJS, 200, 13
Brammer, G. B., van Dokkum, P. G., Illingworth, G. D., et al. 2013, ApJL, 765, L2
Brammer, G. B., Whitaker, K. E., van Dokkum, P. G., et al. 2009, ApJL, 706, L173
Brammer, G. B., Whitaker, K. E., van Dokkum, P. G., et al. 2011, ApJ, 739, 24
Brinchmann, J., Pettini, M., & Charlot, S. 2008, MNRAS, 385, 769
Calzetti, D., Armus, L., Bohlin, R. C., et al. 2000, ApJ, 533, 682
Carollo, C. M., Bschorr, T. J., Renzini, A., et al. 2013, ApJ, 773, 112
Cassata, P., Cimatti, A., Kurk, J., et al. 2008, A&A, 483, L39
Chabrier, G. 2003, PASP, 115, 763
Coil, A. L., Aird, J., Reddy, N., et al. 2015, ApJ, 801, 35
Coil, A. L., Blanton, M. R., Burles, S. M., et al. 2011, ApJ, 741, 8
Coil, A. L., Georgakakis, A., Newman, J. A., et al. 2009, ApJ, 701, 1484
Colless, M., Dalton, G., Maddox, S., et al. 2001, MNRAS, 328, 1039
Conroy, C., Gunn, J. E., & White, M. 2009, ApJ, 699, 486
Cooper, M. C., Griffith, R. L., Newman, J. A., et al. 2012, MNRAS, 419, 3018
Davis, M., Guhathakurta, P., Konidaris, N. P., et al. 2007, ApJL, 660, L1
Domínguez, A., Siana, B., Brooks, A. M., et al. 2014, arXiv:1408.5788
Domínguez, A., Siana, B., Henry, A. L., et al. 2013, ApJ, 763, 145
Donley, J. L., Koekemoer, A. M., Brusa, M., et al. 2012, ApJ, 748, 142
Dutton, A. A., van den Bosch, F. C., Faber, S. M., et al. 2011, MNRAS, 410, 1660
Erb, D. K., Shapley, A. E., Pettini, M., et al. 2006, ApJ, 644, 813
Förster Schreiber, N. M., Genzel, R., Bouché, N., et al. 2009, ApJ, 706, 1364
Genzel, R., Newman, S., Jones, T., et al. 2011, ApJ, 733, 101
Giavalisco, M., Ferguson, H. C., Koekemoer, A. M., et al. 2004, ApJL, 600, L93
Grogin, N. A., Kocevski, D. D., Faber, S. M., et al. 2011, ApJS, 197, 35
Hasinger, G., Miyaji, T., & Schmidt, M. 2005, A&A, 441, 417
Hopkins, A. M., & Beacom, J. F. 2006, ApJ, 651, 142
Horne, K. 1986, PASP, 98, 609
Juneau, S., Dickinson, M., Alexander, D. M., & Salim, S. 2011, ApJ, 736, 104
Kennicutt, R. C., Jr. 1998, ARA&A, 36, 189
Kimura, M., Maihara, T., Iwamuro, F., et al. 2010, PASJ, 62, 1135
Koekemoer, A. M., Faber, S. M., Ferguson, H. C., et al. 2011, ApJS, 197, 36
Kong, X., Charlot, S., Brinchmann, J., & Fall, S. M. 2004, MNRAS, 349, 769
Kriek, M., & Conroy, C. 2013, ApJL, 775, L16
Kriek, M., Labbé, I., Conroy, C., et al. 2010, ApJL, 722, L64
Kriek, M., Labbé, I., van Dokkum, P. G., Franx, M., & Illingworth, G. D. 2008a, ApJ, 682, 896
Kriek, M., van Dokkum, P. G., Franx, M., Illingworth, G. D., & Magee, D. K. 2009a, ApJL, 705, L71
Kriek, M., van Dokkum, P. G., Franx, M., et al. 2008b, ApJ, 677, 219
Kriek, M., van Dokkum, P. G., Labbé, I., et al. 2009b, ApJ, 700, 221
Law, D. R., Steidel, C. C., Erb, D. K., et al. 2009, ApJ, 697, 2057
Lawrence, A., Warren, S. J., Almaini, O., et al. 2007, MNRAS, 379, 1599
le Fèvre, O., Vettolani, G., Garilli, B., et al. 2005, A&A, 439, 845
Lilly, S. J., le Fèvre, O., Renzini, A., et al. 2007, ApJS, 172, 70
Liu, X., Shapley, A. E., Coil, A. L., Brinchmann, J., & Ma, C.-P. 2008, ApJ, 678, 758
Mannucci, F., Cresci, G., Maiolino, R., et al. 2009, MNRAS, 398, 1915
McLean, I. S., Steidel, C. C., Epps, H., et al. 2010, SPIE, 7735
McLean, I. S., Steidel, C. C., Epps, H. W., et al. 2012, SPIE, 8446

Moustakas, J., Zaritsky, D., Brown, M., et al. 2011, arXiv:1112.3300
Muzzin, A., Marchesini, D., Stefanon, M., et al. 2013a, ApJS, 206, 8
Muzzin, A., Marchesini, D., Stefanon, M., et al. 2013b, ApJ, 777, 18
Newman, A. B., Ellis, R. S., Bundy, K., & Treu, T. 2012a, ApJ, 746, 162
Newman, J. A., Cooper, M. C., Davis, M., et al. 2013, ApJS, 208, 5
Newman, S. F., Genzel, R., Förster-Schreiber, N. M., et al. 2012b, ApJ, 761, 43
Oke, J. B., & Gunn, J. E. 1983, ApJ, 266, 713
Osterbrock, D. E. 1989, Astrophysics of Gaseous Nebulae and Active Galactic
    Nuclei (Mill Valley, CA: Univ. Science Books)
Price, S. H., Kriek, M., Brammer, G. B., et al. 2014, ApJ, 788, 86
Quadri, R. F., Williams, R. J., Lee, K.-S., et al. 2008, ApJL, 685, L1
Reddy, N., Dickinson, M., Elbaz, D., et al. 2012a, ApJ, 744, 154
Reddy, N. A., Erb, D. K., Pettini, M., Steidel, C. C., & Shapley, A. E. 2010,
    ApJ, 712, 1070
Reddy, N. A., Pettini, M., Steidel, C. C., et al. 2012b, ApJ, 754, 25
Reddy, N. A., Steidel, C. C., Erb, D. K., Shapley, A. E., & Pettini, M. 2006,
    ApJ, 653, 1004
Reddy, N. A., Steidel, C. C., Pettini, M., et al. 2008, ApJS, 175, 48
Sanders, R. L., Shapley, A. E., Kriek, M., et al. 2015, ApJ, 799, 138
Scoville, N., Aussel, H., Brusa, M., et al. 2007, ApJS, 172, 1
Shapley, A. E. 2011, ARA&A, 49, 525
Shapley, A. E., Coil, A. L., Ma, C.-P., & Bundy, K. 2005, ApJ, 635, 1006
Shapley, A. E., Reddy, N. A., Kriek, M., et al. 2015, ApJ, 801, 88
Shapley, A. E., Steidel, C. C., Pettini, M., & Adelberger, K. L. 2003, ApJ,
    588, 65
Sharples, R. M., Bender, R., Lehnert, M. D., et al. 2004, SPIE, 5492, 1179

Siana, B., Smail, I., Swinbank, A. M., et al. 2009, ApJ, 698, 1273
Silverman, J. D., Kashino, D., Arimoto, N., et al. 2014, arXiv:1409.0447
Skelton, R. E., Whitaker, K. E., Momcheva, I. G., et al. 2014, ApJS, 214, 24
Steidel, C. C., Adelberger, K. L., Shapley, A. E., et al. 2003, ApJ, 592, 728
Steidel, C. C., Shapley, A. E., Pettini, M., et al. 2004, ApJ, 604, 534
Steidel, C. C., Rudie, G. C., Strom, A. L., et al. 2014, ApJ, 795, 165
Tremonti, C. A., Heckman, T. M., Kauffmann, G., et al. 2004, ApJ, 613, 898
van de Sande, J., Kriek, M., Franx, M., et al. 2013, ApJ, 771, 85
van Dokkum, P. G. 2001, PASP, 113, 1420
van Dokkum, P. G., Brammer, G., Fumagalli, M., et al. 2011, ApJL,
    743, L15
van Dokkum, P. G., Leja, J., Nelson, E. J., et al. 2013, ApJL, 771, L35
van Dokkum, P. G., Whitaker, K. E., Brammer, G., et al. 2010, ApJ, 709, 1018
Whitaker, K. E., Kriek, M., van Dokkum, P. G., et al. 2012, ApJ, 745, 179
Whitaker, K. E., Labbé, I., van Dokkum, P. G., et al. 2011, ApJ, 735, 86
Whitaker, K. E., van Dokkum, P. G., Brammer, G., et al. 2013, ApJL, 770,
    L39
Williams, R. J., Quadri, R. F., Franx, M., van Dokkum, P., & Labbé, I. 2009,
    ApJ, 691, 1879
Williams, R. J., Quadri, R. F., Franx, M., et al. 2010, ApJ, 713, 738
Wisnioski, E., Förster Schreiber, N. M., Wuyts, S., et al. 2015, ApJ, 799, 209
Wuyts, S., Förster Schreiber, N. M., Lutz, D., et al. 2011b, ApJ, 738, 106
Wuyts, S., Förster Schreiber, N. M., van der Wel, A., et al. 2011a, ApJ, 742, 96
Wuyts, S., Labbé, I., Franx, M., et al. 2007, ApJ, 655, 51
Yan, R., Ho, L. C., Newman, J. A., et al. 2011, ApJ, 728, 38
York, D. G., Adelman, J., Anderson, J. E., Jr., et al. 2000, AJ, 120, 1579